A PROBABILISTIC APPROACH FOR MULTISCALE POROELASTIC MODELING OF MATURE ORGANIC-RICH SHALES

A Thesis

by

MOHAMMAD MASHHADIAN

Submitted to the Office of Graduate and Professional Studies of
Texas A&M University
in partial fulfillment of the requirements for the degree of

MASTER OF SCIENCE

Chair of Committee,	Arash Noshadravan
Co-chair of Committee,	Sara Abedi
Committee Member,	Zachary Grasley
Head of Department,	Robin Autenrieth

August 2017

Major Subject: Civil Engineering

ABSTRACT

Organic-rich shales have been recognized as one of the most important energy resources in the world due to their ubiquitous presence. However, there are numerous engineering challenges serving as obstacles for exploiting these geo-materials with multi-scale microstructure. This work addresses an important aspect of engineering challenges in understanding the complex behavior of organic-rich source rocks, namely their anisotropic poroelastic behavior at multiple scales.

To this end, we utilize a framework obtained by combining experimental characterization, physically-based modeling and uncertainty quantification that spans and integrates scales from nanoscale to macroscale. The multiscale models play a crucial role in predicting macroscale mechanical properties of organic-rich shales based on the available information on poromechanical properties in microscale. Recently a three-level multiscale model has been developed that spans from the nanometer length scale of organic-rich shales to the scale of macroscopic composite. This approach is powerful in capturing the homogenized/effective properties/behavior of these geomaterials. However, this model ignores the fluctuation/uncertainty in mechanical and compositional model parameters. As such the robustness and reliability of these estimates can be questioned in view of different sources of uncertainty, which in turn affect the requisite information based on which the models are constructed. In this research, we aim to develop a framework to systematically incorporate the main sources of uncertainty in modeling the multiscale behavior of organic-rich shales, and thus take the existing model one step

forward. Particularly, we identify and model the uncertainty in main model parameters at each scale such as porosity and elastic properties. To that end, maximum entropy principle and random matrix theory are utilized to construct probabilistic descriptions of model parameters based on available information. Then, to propagate uncertainty across different scales the Monte Carlo simulation is carried out and consequently probabilistic descriptions of macro-scale properties are constructed. Furthermore, a global sensitivity analysis is carried out to characterize the contribution of each source of uncertainty on the overall response. Finally, methodological developments will be validated by both simulation and experimental test database.

DEDICATION

This work is dedicated to my family for their

unconditional love, and support

throughout my life.

ACKNOWLEDGEMENTS

I would like to express my gratitude to my thesis advisor Dr. Arash Noshadravan, and co-advisor Dr. Sara Abedi for their continuous support, patience, and guidance during the course of my graduate study at Texas A&M University. I have cherished every one of our discussions as they were full of insights and encouragement.

Thanks also go to my friends and colleagues and the department faculty and staff for making my time at Texas A&M University a great experience.

Finally, thanks to my parents for their support during my graduate study in United States.

CONTRIBUTORS AND FUNDING SOURCES

Contributors

This work was supervised by a thesis committee consisting of Dr. Arash Noshadravan (advisor) and Dr. Zachary Grasley of the Department of Civil Engineering and Dr. Sara Abedi (co-advisor) of the Department of Petroleum Engineering.

All work conducted for the thesis was completed by the student independently.

Funding Sources

There are no outside funding contributions to acknowledge related to the research and compilation of this document.

TABLE OF CONTENTS

LIST OF FIGURES

LIST OF TABLES

1 INTRODUCTION

1.1 Overview

The term shale has been used in two categories from a historical point of view: 1) as a general group-name for all fine-grained siliciclastic rocks, and 2) as a definition of laminated clayey rocks [Tourtelot 1960]. In this work, we investigate shale materials from a geomechanics point of view. From this perspective, shale materials are considered as a sedimentary rock, composed of small-size particles (less than 4 μm in diameter of characteristic length, but may include silt-size particles of 62.5 μm) [Passey 2010].

Organic-rich shales are multiphase, ultra-low permeable geo-materials which exhibit multi-scale microstructure [Dormieux et al. 2006], and can be classified into two groups: mature and immature. The rate of maturation is a function of time, temperature and pressure. Organic maturity processes during burial stages are classified as [Monfared 2015]:

- *Diagenesis:* **"**This process is associated with biogenic decay, catalyzed by bacteria and abiogenic reactions which occur in shallow depths with normal temperatures and pressures. During this process, methane, carbon dioxide, and water are given off by the originally deposited organic matter, leaving behind what is called kerogen. In this process, oxygen content is reduced, leaving the Hydrogen: Carbon ratio (H:C) unchanged".
- *Catagenesis:* "This phase is linked to petroleum release from kerogen as burial continues and subsequent pressure and temperature increases, first oil and later gas is generated. During this stage, the Hydrogen: Carbon (H:C) ratio decreases while the Oxygen: Carbon (O:C) ratio remains mainly intact".

- *Metagenesis:* "This phase occurs at high pressure and high temperature environments (HP/HT). During this process, the last hydrocarbons (HC), generally methane, are expelled. The H:C ratio keeps decreasing until the Carbon left is in the form of graphite".

Organic-rich shales serve as main sealing formations in petroleum reservoirs [Mavko et al. 2009], and are used in nuclear waste storage [Andra 2005, Ortega et al. 2007, Sarout and Guéguen 2008]. Also, these rocks play a critical role as a source of energy based on a recently published report by Energy Information Administration (EIA) [World Energy Council (2007)]. However, their anisotropic poroelastic behavior at multiple length scales pose one of the most intricate challenges to the recovery of these hydrocarbon reservoirs. There are two main ideas about sources of anisotropy in shales: the first group attribute anisotropy to the geometric factors, i.e. particle shapes and orientation, which can be obtained through advanced imaging techniques [Hornby et al 1994, Sayers 2005]. The second school of thoughts believe that the main source of shale's anisotropy behavior is due to the intrinsic anisotropy of shale's building block, namely clay minerals [Ortega et al. 2007, Ortega et al. 2009].

The content and spatial distribution of different phases/materials forming organic-rich shales, mainly pores, clay minerals, organic content and silt inclusions, impact the elastic and poroelastic behavior of organic rich shales [Cosenza et al. 2015]. Hence, knowledge of the microstructure of these porous organic/inorganic composites is critical in predicting the elastic and poroelastic behavior of them.

Different researchers have investigated the role of microstructure in elastic and poroelastic characteristics of shales which can be categorized into two groups [Cosenza et al. 2015]:

- In the first group, through employing imaging techniques and advanced X-ray diffraction the estimated microstructural pattern of shales is obtained which ultimately is used in characterizing bulk elastic properties of shales [Hornby et al. 1994, Sayers 1994, Robinet et al. 2012, Vasin et al. 2013].
- In the second group, different effective medium approximations are employed to introduce a homogenized elastic property of shales at a given microstructure level [Giraud et al. 2007, Monfared and Ulm 2016].

The second group of approaches take a step forward to overcome the expensive and time-consuming experiments to obtain the mechanical behavior of shales, however, they have been utilized within a deterministic framework and as such does not account for the uncertainty in compositional and mechanical model parameters. Incorporating uncertainty into predictive mechanical models is a key factor in improving the robustness and reliability of the model predictions which has been employed for different materials such as bone [Sansalone et al. 2016], but it has not been used in multiscale predictive poroelastic models of shales.

1.2 Research Motivation

The goal of this research is to incorporate uncertainty in modeling behavior of mature organic-rich shales by considering the uncertainty in main subscale features. A

probabilistic model that links microtexture to anisotropic poroelasticity and seismic properties of organic-rich shales is valuable in many fields of petroleum engineering. Physical rock parameters can be inferred from seismic data inversion using this model. This information can be utilized to produce spatial distribution of various physical properties in the 3D volume of a target formation by integrating them into a geo-model. Knowing such models and uncertainty associated with them, a reservoir engineer can forecast reservoir performance with higher confidence. Furthermore, developed elastic property maps can be employed to estimate the spatial variation of energy release rates as a robust way to assess fracability of the formation of interest, accounting for organic-rich shale heterogeneity and anisotropic poroelasticity.

1.3 Objectives

We aim to extend and improve a recently developed multiscale model for organic-rich shale and introduce uncertainty to its input parameters through a systematic approach to construct probabilistic model of input parameters to the model based on available information, and then propagate the uncertainties over different length scales of the model and consequently obtain probabilistic descriptions of macroscale quantities of interest. The framework utilized to achieve this goal comprises experimental characterization, microporomechanical modeling and uncertainty quantification and propagation which is of great value. Utilizing this framework, the prediction and identification of essential quantities of interest in engineering scale, such as acoustic properties, is improved in terms of robustness. Three primary research objectives guide this research:

1. Extending and improving a recently developed multiscale model for predicting the poroelastic behavior of organic-rich shales. To this end, we employed a multiscale structure thought model developed by Abedi et al. (2016b) and improved it in order to make it suitable for mature organic-rich shales.
2. Identifying and characterizing the most important uncertain input parameters to the multiscale model, and developing the required statistics for those parameters based on available information. In order to achieve this goal, after identifying the uncertain parameters, required statistics are developed through a systematic framework of random matrix theory and Maximum Entropy Principle.
3. Propagating the uncertainty across different length scales and subsequently constructing probabilistic descriptions of quantities of interest at different length scales. The Monte Carlo simulation is carried out to propagate uncertainties, and ultimately construct the probabilistic description of poroelastic properties.

1.4 Thesis Outline

Following the introduction chapter, chapter 2 addresses acquiring a multiscale thought model for mature organic-rich shale, which will be used as a basis for the subsequent developments. Chapter 3 is dedicated to introducing the experimental settings used in order to mechanically characterize the samples of mature organic-rich shales. For macroscopic characterization of samples Ultrasonic Pulse Velocity (UPV), and for the

microscopic characterization of the samples instrumented nanoindentation is utilized. Chapter 4 develops the basic micromechanics tools which will be used in subsequent model development, such as theory of homogenization, self-consistent scheme as an approximation method for homogenization, and modeling of imperfect interfaces. Chapter 5 utilizes developed tools in chapter 4 to develop a multiscale model for mature organic-rich shale. Chapter 6 is dedicated to the uncertainty quantification of uncertain input parameters, incorporating them with the developed model in chapter 5, and propagating them through multiple length scales. To this end, maximum entropy principle and random matrix theory are employed. Chapter 7 presents the calibration and validation processes of the multiscale model. Also, a sensitivity analysis is conducted in this chapter to quantify the sensitivity of model output to the uncertain input parameters. Finally, chapter 8 is dedicated to a summary of findings, followed by limitations of this work and future prospective.

1.5 Notations

Throughout this work, fourth-order tensors are denoted by $[\![A]\!]$, and second order tensors are denoted by $[A]$. Specific notations for a chapter are introduced at the beginning of the chapter.

It is assumed that mature organic-rich shale exhibits a transversely isotropic behavior at all different length scales. To develop the multiscale model in the subsequent chapters, a Cartesian coordinate system is adopted where axis x_3 is perpendicular to the plane of isotropy (bedding plane), and x_1 and x_2 are parallel to the plane of isotropy. Also, the

stiffness tensor for a transversely isotropic medium, in Voigt's notation, is defined as [Cowin 2003, and Cowin and Mehrabadi 1992]:

$$[C] = \begin{bmatrix} C_{11} & C_{12} & C_{13} & 0 & 0 & 0 \\ C_{12} & C_{11} & C_{13} & 0 & 0 & 0 \\ C_{13} & C_{13} & C_{33} & 0 & 0 & 0 \\ 0 & 0 & 0 & 2C_{66} & 0 & 0 \\ 0 & 0 & 0 & 0 & 2C_{44} & 0 \\ 0 & 0 & 0 & 0 & 0 & 2C_{44} \end{bmatrix} \tag{1.1}$$

where $C_{66} = \frac{C_{11} - C_{12}}{2}$

2 HIERARCHIAL PRESENTATION OF MATURE ORGANIC-RICH SHALES

In this chapter, the multiscale thought model of mature organic-rich shale is introduced, which will be employed in future chapters in order to develop a model to capture the microporoelastic behavior of mature-organic rich shale. This model addresses both the structure and the morphology of mature organic-rich shale at different length scales.

2.1 Multiscale Thought Model of Mature Organic-Rich Shale

Following multiscale thought model is inspired by the work of Abedi et al. 2016b, and will be used as a basis for future development of probabilistic multiscale model of mature organic-rich shale.

2.1.1 Level 0

This level has been considered as the building block of organic-rich shale and is fundamental scale of clay mineralogy (e.g. illite, kaolinite, etc.). Due to small nature of clay minerals, their platy geometry, and their high affinity for water [Ebrahimi et al. 2012], direct measurement of stiffness of a single clay crystal at this level is a formidable task. Clay is assumed to represent a transversely isotropic behavior at this level with a stiffness tensor of $[\![C^{clay}]\!]$, and is considered as the sole source of anisotropy behavior of shale at different length scales in our model.

2.1.2 Level I

Level I represents porous organic/clay composite at the micrometer length scale with a drained stiffness tensor of $[\![C_{hom}^{I}]\!]$, and undrained stiffness tensor of $[\![C_{hom}^{I,un}]\!]$. At this level, advanced observational methods (e.g. SEM) and nanoindentaion measurements are carried out [Babko et al. 2011; Abedi et al. 2016a].

2.1.3 Level II

This level consists of porous clay/organic fabric intermixed with poorly sorted silt inclusions of characteristic size of millimeter and sub-millimeter range, and is represented with a drained stiffness tensor of $[\![C_{hom}^{II}]\!]$, and undrained stiffness tensor of $[\![C_{hom}^{II,un}]\!]$. This is the level of acoustic and classical strength of materials measurements [Ortega et al. 2007, Bobko et al. 2011].

It has been shown that as kerogen matures, morphology of organic-rich shale changes, from a connected network of kerogen to a disperse distribution of kerogen pockets in the background matrix [Prasad et al 2009, Ahmadov 2011]. Also, some works by researchers such as Vernik and Lnadis (1996), and Vernik and Liu (1997) suggest that discontinuities in mature organic-rich shales are prevalent relative to the immature shales. Weakened interfaces are introduced between equivalent inclusion grains and their surrounding matrix in the mature organic-rich shales to account for the presence of these discontinuities. This weakened/imperfect interfaces are modeled through employing Interfacial Transition Zones (ITZs) which will be addressed in the chapter 4. The term equivalent inclusion is utilized for the newly defined phase which is obtained from homogenization of different inclusion grains.

Figure 2.1 schematically represents the multiscale thought model employed for the mature organic-rich shale.

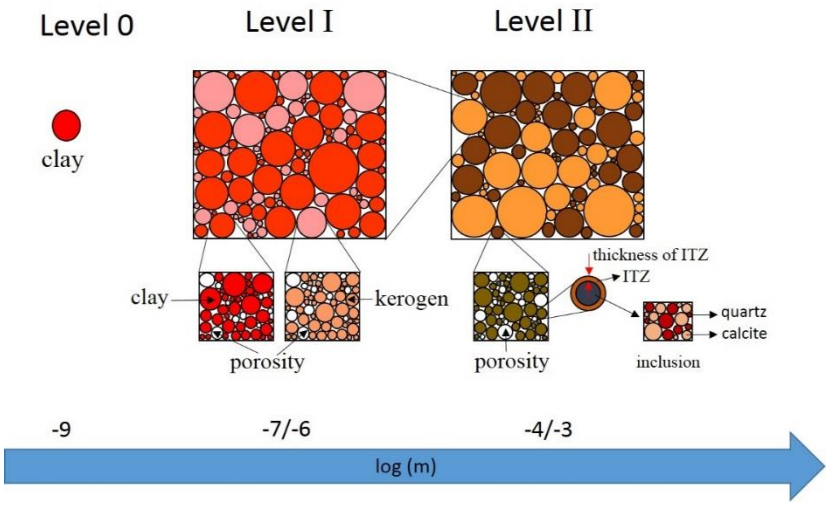

Fig. 2.1 Multiscale structure thought model developed for mature organic-rich shale

2.2 Chapter Summary

This chapter presented a multiscale thought model of mature organic-rich shale which is suitable from structural and morphological points of view. This model consists of three length scales/levels: level 0 which is the level of consolidated clay; level I which is the level of porous organic/clay mixture and indentation measurements are performed at this level; and level II which is the level of porous clay/organic fabric intermixed with silt inclusions. This model, considers the role of maturity in the morphology of organic rich shales, and suggest a mechanism (weakened interface) to account for discontinuities which are a ramification of maturity.

3 MATERIAL CHARACTERIZATION AND PROPERTIES

To develop the probabilistic microporomechanics model, two groups of datasets are used at each of the two length scales: microscale and macroscale with characteristic sizes of sub-micrometer and sub-millimeter/ millimeter ranges, respectively. One dataset at each length scale is used for model calibration and the other dataset is used for model validation. At the micrometer length scale, datasets contain the indentation moduli of nanoindentation test for the shale samples in the dataset. At the macroscale, datasets contain five independent components of shale samples which are obtained through Ultrasonic Pulse Velocity (UPV) measurement.

3.1 Ultrasonic Pulse Velocity Measurement

In this technique the travel time of elastic compressional (P-) and shear (S-) waves, which are generated by piezoceramic elements with central frequencies in the MHz range, through a rock sample for a known wave-path length is measured. These velocities are used to identify the five independent components of undrained elasticity tensor of shale samples at macroscale. Based on the elastic waves theory in a transversely isotropic medium, for the velocity of waves propagating in the plane of isotropy we get:

$V_{S1} = \sqrt{\frac{C_{66}}{\rho}}$; pure shear mode polarized normal to the symmetry axis (x_3) (3.1a)

$V_{S3} = \sqrt{\frac{C_{44}}{\rho}}$; pure shear mode polarized parallel to the symmetry axis (x_3) (3.1b)

$V_{P1} = \sqrt{\frac{C_{11}}{\rho}}$; pure longitudinal mode (3.1c)

where ρ is the mass density of material, subscript "s" denotes shear wave and subscript "p" denotes compression wave, and numbers in the subscript denote direction of the propagation. In this case, wave velocities are independent of the propagation direction in the plane of isotropy. Also, for the waves propagating parallel to the symmetry axis we get [Ortega 2010]:

$V_{S3} = \sqrt{\frac{C_{44}}{\rho}}$; pure shear mode polarized normal to the symmetry axis (3.2a)

$V_{P3} = \sqrt{\frac{C_{33}}{\rho}}$; pure longitudinal mode (3.2b)

Thus, to obtain the components of undrained elasticity tensor at level II from UPV measurement, one can use following set of equations [Ortega 2010]:

$C_{11}^{UPV} = \rho V_{P1}^2$ (3.3a)

$C_{33}^{UPV} = \rho V_{P3}^2$ (3.3b)

$C_{66}^{UPV} = \rho V_{S1}^2 = \frac{(C_{11}^{UPV} - C_{12}^{UPV})}{2}$ (3.3c)

$C_{44}^{UPV} = \rho V_{S3}^2$ (3.3d)

$C_{13}^{UPV} = -C_{44} + \alpha\sqrt{(C_{11} + C_{44} - 2\rho V_{qP45}^2)(C_{33} + C_{44} - 2\rho V_{qP45}^2)}$ (3.3e)

where

V_{qP45} = quasi-longitudinal ($\alpha = +1$) or quasi-shear wave ($\alpha = -1$).

3.2 Instrumented Nanoindentation

In this test, an indenter tip of known mechanical and geometric properties is pressed perpendicularly to the surface of the material under experiment. The load P and the depth h are recorded during the test (P is the load applied to the indenter, and h is the depth of the indenter with respect to the initial material surface). The characteristic mechanical response of the tested material can be defined through the $P-h$ curve (See Fig. 1), and using following equation:

$$\mathrm{M}=\frac{\sqrt{\pi}}{2}\frac{\mathrm{S}}{\sqrt{A_c}} \tag{3.4}$$

where A_c is the projected contact area between intender tip and the surface of the sample, and $\mathrm{S}=\frac{\mathrm{d}P}{\mathrm{d}h}$ is the initial slop of the unloading portion of the load-displacement ($P-h$) curve. For the mature organic-rich shale with a transversely isotropic behavior, indentation moduli can be expressed in terms of components of $[\![C_{hom}^{I}]\!]$ as [Delafargue and Ulm 2004]:

$$\mathrm{M}_3=2\sqrt{\frac{C_{11}C_{33}-{C_{13}}^2}{C_{11}}\left(\frac{1}{C_{44}}+\frac{2}{\sqrt{C_{11}C_{33}+C_{13}}}\right)^{-1}} \tag{3.5a}$$

$$\mathrm{M}_1\approx\sqrt{\sqrt{\frac{C_{11}}{C_{33}}}\frac{{C_{11}}^2-{C_{12}}^2}{C_{11}}\mathrm{M}_3} \tag{3.5b}$$

where $C_{ij}s$ are the components of $[\![C_{hom}^{I}]\!]$, and M_1 and M_3 represent indentation moduli in x_1 and x_3 directions, respectively.

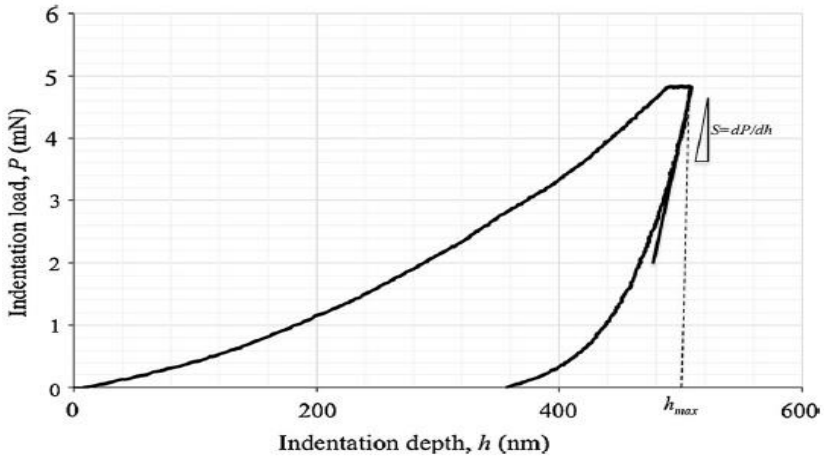

Fig. 3.1 Typical indentation curve obtained by nanoindentation

3.3 Calibration and Validation Datasets

To calibrate the model and validate the simulations two sets of data at level I and two sets of data at level II are utilized. At level I, two data sets comprise calibration data set 1 (CDS1) and validation data set 1 (VDS1) which are reported in Table 7.1 and Table 7.5, respectively. At level II, calibration data set 2 (CDS2) reported in Table 7.2 and validation data set 2 (VDS2) presented in Table 7.7 form the two data sets at this level.

CDS1 comprises indentation moduli of samples from Marcellus (108, 150 and 151) and Fayetteville (Fay) which are utilized to calibrate the model at level I and level 0. VDS1 contains measured indentation moduli of samples from Marcellus (46 and 49) and Haynesville (B2, B5 and B6) and is employed to validate the simulations at level I. Moreover, CDS2 includes the undrained elasticity components of samples from Haynesville (B1, B2 and B5) which are obtained through UPV measurements. These elasticity components are used to calibrate the model at level II. Finally, VDS2 contains

undrained elasticity components of samples from Haynesville (B3, B4 and B6) which is employed to validate the simulations at level II.

Table 3.1 represents the mineralogy, organic content and porosity of Haynesville shale samples (B1, B2, B3, B4, B5, and B6). In this study, densities of 2.65 g/cm^3 for quartz and feldspar, 2.71 g/cm^3 for carbonates, 2.65-2.82 g/cm^3 for clay and 1.2 g/cc for kerogen are considered [Abedi et al. 2016a]. Table 3.2 represents the volume fractions of clay and kerogen and porosity at level I for samples from Marcellus (46, 49, 108, 150, and 151) and Fayetteville (Fay).

Table 3.1- Mineralogy and organic content of shale samples

Measured Quantities	**B1**	**B2**	**B3**	**B4**	**B5**	**B6**
Quartz (mass %)	30	27	16	20	32	28
Feldspar (mass %)	7	9	5	6	11	10
Carbonate (mass %)	30	22	65	51	9	12
Clay (mass %)	30	38	11	20	43	38
Kerogen (mass %)	2.48	3.34	1.57	2.65	3.3	3.16
$\boldsymbol{\phi}$ **(porosity) (%)**	6.64	7.36	4.61	5.57	7.16	7.59

Table 3.2- Volume fraction of shale samples at level I

Measured Quantity	**46**	**49**	**108**	**150**	**151**	**Fay**
Clay (%)	0.8914	0.8688	0.6855	0.6776	0.6473	0.669
Kerogen (%)	0.0246	0.0522	0.2425	0.2634	0.2877	0.291
$\boldsymbol{\phi}$ **(%)**	0.084	0.079	0.072	0.059	0.065	0.04

Table 3.3 contains the isotropic elasticity of carbonate, quartz, and feldspar which is characterized by their bulk (K) and shear (G) modulus.

Table 3.3- Isotropic elasticity of different minerals

Phase	$\boldsymbol{K(GPa)}$	$\boldsymbol{G(Gpa)}$
$\boldsymbol{Calcite}$	58.2	28.3
$\boldsymbol{Quartz}$	37.9	44.3
$\boldsymbol{Feldspar}$	62	29.3

In the multiscale model which will be developed in the subsequent chapters, it is considered that feldspar is mechanistically represented by calcite, in terms of elasticity. The reason for the choice is that elasticity of calcite and feldspar are similar to each other.

3.4 Chapter Summary

This chapter briefly explains the mechanism of UPV measurement which is used to determine the undrained elasticity of shale samples at Level II, as well as instrumented indentation which is employed to inform us about the elasticity properties of shale samples at Level I. Furthermore, a set of shale samples is presented in this chapter which will be used to calibrate and validate multiscale model at multiple length scales in the following chapters.

4 BASIS OF MICROPOROMECHANICS

The goal of this chapter is to develop a framework to compute the homogenized response of a heterogeneous material at different length scales. Different computational and theoretical methods have been developed to model heterogeneous materials such as finite element theory. One of the options in modeling heterogeneous materials is using analytical approaches where continuum mechanics and random homogenization theory are employed. In this chapter, a framework of inclusion-based effective medium theories is employed to estimate the effective composite response. All the developments in this chapter are obtained within the framework of linear microporoelasticity.

4.1 Representative Elementary Volume (REV)

Before implementing the tools of continuum mechanics, we need to define Representative Elementary Volume (*REV*), and ensure that scale separability conditions, which allow the usage of continuum mechanics tools, are met. *REV* is an infinitesimal part of a material system consists of r subdomains of micro-homogeneous phases ($\Omega = \bigcup_{i=1}^{r} \Omega_i$) with a characteristic length scale (l). Length scale (l) of *REV* has to meet following inequalities known as scale separability conditions:

$$d0 << d << l << L \tag{4.1a}$$

$$L << \lambda \tag{4.1b}$$

where:

L: characteristic length scale of the material system

d: characteristic length scale of local heterogeneities (condition $d<<l$ is for *REV* to be representative of the system and capture the properties of the system which are relevant in the behavior modeling)

$d0$: lower bound for the continuum mechanics to be applicable

λ: load fluctuation length

4.2 Concentration or Localization

By relating a macroscale strain or stress field to its microscale counterpart, through solving a boundary value problem, one can obtain the constitutive model. Modeling of the local stress and strain fields ($\boldsymbol{\sigma}(\mathbf{x})$, $\boldsymbol{\varepsilon}(\mathbf{x})$) of the mechanical phases in the *REV* from the prescribed macroscopic stress and strain quantities $\boldsymbol{\Sigma}$, $\boldsymbol{E}$ is investigated in this part. Since constraints at the boundary of *REV* are not known, we consider Hashin boundary conditions where boundary conditions on the *REV* are homogeneous.

If *REV* is subjected to a constant macroscopic stress ($\boldsymbol{\Sigma}$), *uniform stress boundary condition* is considered:

$$\boldsymbol{\sigma}(\mathbf{x}).n(\mathbf{x}) = \boldsymbol{\Sigma}.n(\mathbf{x}) \tag{4.2}$$

where n is the unit outward normal to the boundary of the *REV*. Also, if *REV* is subjected to a uniform displacement, *uniform strain boundary condition* is considered:

$$\xi(\mathbf{x}) = \boldsymbol{E}.\mathbf{x} \tag{4.3}$$

where $\xi(\mathbf{x})$ represents the uniform displacement. It can be shown that $\boldsymbol{\Sigma}$ is equivalent to the volume average of the divergence free stress in the *REV, and* $\mathbf{E}$ is equivalent to the volume average of the strain field in *REV*. So:

$$< \boldsymbol{\sigma} >_{\Omega} = \frac{1}{|\Omega|} \int_{\Omega} \boldsymbol{\sigma}(\mathbf{x})\, dV_{\mathbf{x}} = \boldsymbol{\Sigma} \tag{4.4}$$

$$< \boldsymbol{\varepsilon} >_{\Omega} = \frac{1}{|\Omega|} \int_{\Omega} \boldsymbol{\varepsilon}(\mathbf{x})\, dV_{\mathbf{x}} = \boldsymbol{E} \tag{4.5}$$

where $< \cdots >$ stands for volume averaging. The consequence of applying uniform boundary condition is Hill lemma which states that the macroscopic strain energy is equal to microscopic strain energy [Dormieux et al. 2006]:

$$< \boldsymbol{\sigma} : \boldsymbol{\varepsilon} > = < \boldsymbol{\sigma} > : < \boldsymbol{\varepsilon} > = \boldsymbol{\Sigma} : \boldsymbol{E} \tag{4.6}$$

Considering Hill lemma, we can express microscopic stress and strain fields (at each phase) as functions of the applied macroscopic boundary conditions:

$$\boldsymbol{\sigma}(\mathbf{x}) = \mathfrak{B}(\boldsymbol{\Sigma}) \tag{4.7a}$$

$$\boldsymbol{\varepsilon}(\mathbf{x}) = \mathbb{A}(\boldsymbol{\Sigma}) \tag{4.7b}$$

4.3 Homogenization

The goal of homogenization is to find the expression for $\boldsymbol{E}$, macroscopic strain, associated with the $\boldsymbol{\varepsilon}(\mathbf{x})$, microscopic strain field, when the *REV* is subjected to a macroscopic loading $\boldsymbol{\Sigma}$. Equivalently, the relation between the macroscopic stress $\boldsymbol{\Sigma}$ and the microscopic stress field $\boldsymbol{\sigma}(\mathbf{x})$ is sought when the *REV* is subjected to a macroscopic strain $\boldsymbol{E}$. So, we have:

$$\boldsymbol{E}(\boldsymbol{\Sigma}) = < \boldsymbol{\varepsilon}(\boldsymbol{\sigma}) >_{\Omega} = < \boldsymbol{\varepsilon}(\mathfrak{B}(\boldsymbol{\Sigma})) >_{<\Omega>} \tag{4.8a}$$

$$\boldsymbol{\Sigma}(\boldsymbol{E}) = < \boldsymbol{\sigma}(\varepsilon) >_{\Omega} = < \boldsymbol{\sigma}(\mathbb{A}(\boldsymbol{\Sigma})) >_{<\Omega>} \tag{4.8b}$$

In the linear elasticity case, the microscopic and macroscopic stresses and strains are related by a fourth-order concentration tensor to the loading parameters $\boldsymbol{E}$ and $\boldsymbol{\Sigma}$ [Zaoui 2002]. So (at each phase),

$$\boldsymbol{\sigma}(\mathbf{x}) = [\![\mathrm{B}(\mathbf{x})]\!] : \boldsymbol{\Sigma} \quad (for\ all\ \mathbf{x} \in \Omega) \tag{4.9a}$$

$$\boldsymbol{\varepsilon}(\mathbf{x}) = [\![\mathrm{A}(\mathbf{x})]\!] : \boldsymbol{E} \quad (for\ all\ \mathbf{x} \in \Omega) \tag{4.9b}$$

where $[\![\mathrm{B}(\mathbf{x})]\!]$ is the fourth-order stress concentration tensor and $[\![\mathrm{A}(\mathbf{x})]\!]$ is the fourth-order strain concentration tensor. For the local stresses, at phase r:

$$\boldsymbol{\sigma}^r(\mathbf{x}) = [\![\mathrm{C}^r(\mathbf{x})]\!] : \boldsymbol{\varepsilon}^r(\mathbf{x}) = [\![\mathrm{C}^r(\mathbf{x})]\!] : [\![A^r(\mathbf{x})]\!] : \boldsymbol{E} \qquad for\ all\ \mathbf{x} \in \Omega^r \tag{4.10}$$

With using the average rule:

$$\boldsymbol{\Sigma} = < \boldsymbol{\sigma}^r(\mathbf{x}) >_{\Omega} = < [\![\mathrm{C}^r(\mathbf{x})]\!] : [\![A^r(\mathbf{x})]\!] : \boldsymbol{E} >_{\Omega} \tag{4.11}$$

So, we identify homogenized stiffness tensor as:

$$[\![\mathrm{C}_{hom}]\!] = < [\![\mathrm{C}^r(\mathbf{x})]\!] : [\![A^r(\mathbf{x})]\!] >_{\Omega} \tag{4.12}$$

It is clear from Eq. (4.12) that determination of $[\![A^r(\mathbf{x})]\!]$ (strain concentration tensor) is critical to the homogenization problem. That's what we aim to obtain in the next section.

4.4 Eshelby's Inclusion Problem

The Eshelby's solution [Eshelby 1957] provides the foundation for estimating concentration tensors that are suitable for particulate and granular microstructure. "Eshelby's problem addresses the strain field in an ellipsoidal inclusion, embedded in an infinite homogeneous medium, with different elasticity, and subjected to uniform displacement boundary" [Ortega 2010]. The problem is presented as:

$$\nabla . \boldsymbol{\sigma} = 0 \qquad (\mathbf{x} \in \Omega)$$

$$\boldsymbol{\sigma}(\mathbf{x}) = [\![C^{mat}]\!] : \boldsymbol{\varepsilon}(\mathbf{x}) + \boldsymbol{\sigma^I}(\mathbf{x}) \qquad (\mathbf{x} \in \Omega) \tag{4.13}$$

$$\xi^1 = \boldsymbol{E} . \mathbf{x} \qquad (\mathbf{x} \to \infty)$$

where $[\![C^{mat}]\!]$ represents the homogeneous/matrix stiffness tensor, and $\boldsymbol{\sigma^I}(\mathbf{x})$ is a stress field that characterizes the deviation from the homogeneous state induced by the inclusion:

$$\boldsymbol{\sigma^I}(x) = \begin{cases} 0 & (for\ all\ \mathbf{x} \in \Omega^{mat}) \\ \delta[\![\mathrm{C}]\!] & (for\ all\ \mathbf{x} \in \Omega^I) \end{cases} \tag{4.14}$$

where $\delta[\![\mathrm{C}]\!] = [\![\mathrm{C}^I]\!] - [\![\mathrm{C}^{mat}]\!]$ is the elasticity contrast between the inclusion and homogeneous matrix. In addition, $\Omega = \Omega^I + \Omega^{mat}$ where Ω^I denotes the domain of inclusion, and Ω^{mat}represents the domain of homogeneous matrix which is not occupied by inclusion. The result of Eshelby's inclusion problem is that the strain field is constant within an ellipsoidal inclusion:

$$\boldsymbol{\varepsilon}^I(\mathbf{x}) = -[\![S^{esh}]\!] : [\![\mathrm{C}^{mat}]\!]^{-1} : \boldsymbol{\sigma}^I(\mathbf{x}) + \boldsymbol{E} \tag{4.15}$$

where $[\![S^{esh}]\!]$ is the Eshelby's tensor. The $\boldsymbol{\sigma}^I(\mathbf{x})$ is also constant in the inclusion, and it is related to the macroscopic strain by:

$$\boldsymbol{\sigma}^I(\mathbf{x}) = [[\![I]\!] + \delta[\![\mathrm{C}]\!] : [\![S^{esh}]\!] : [\![\mathrm{C}^{mat}]\!]^{-1}] : \delta[\![\mathrm{C}]\!] : \boldsymbol{E} \quad (\Omega^I) \tag{4.16}$$

where $[\![I]\!]$ represents the fourth-order identity tensor defined as $[\![I]\!]_{ijkl} = \frac{1}{2}(\delta_{ik}\delta_{jl} + \delta_{il}\delta_{jk})$, and $[\delta]$ denotes the Kronecker delta. Combining Eqs. (4.15) and (4.16) yields:

$$\boldsymbol{\varepsilon}^I = [[\![I]\!] + [\![S^{esh}]\!] : ([\![\mathrm{C}^{mat}]\!]^{-1} : [\![\mathrm{C}^I]\!] - [\![I]\!])]^{-1} : \boldsymbol{E} \qquad (\Omega^I) \tag{4.17}$$

Now, by comparing (4.17) and (4.9b), one can recognize that:

$$[\![\mathrm{A}^I]\!] = [[\![I]\!] + [\![S^{esh}]\!] : ([\![\mathrm{C}^{mat}]\!]^{-1} : [\![\mathrm{C}^I]\!] - [\![I]\!])]^{-1} \tag{4.18}$$

where $[\![A^I]\!]$ is the strain concentration tensor of the macroscopic strain into the inclusion phase. Now, using Eq. (4.18), one can obtain the strain field in the r^{th} phase in response to an imposed homogeneous macroscopic strain field on the boundaries of REV at infinity, $\boldsymbol{E}^{\infty}$, as:

$$\boldsymbol{\varepsilon}^r(\mathbf{x}) = [\![\mathrm{A}^r]\!] : \boldsymbol{E}^{\infty} = [[\![I]\!] + [\![S^{esh}]\!] : ([\![\mathrm{C}^{mat}]\!]^{-1} : [\![\mathrm{C}^r]\!] - [\![I]\!])]^{-1} : \boldsymbol{E}^{\infty} \tag{4.19}$$

where $[\![\mathrm{C}^r]\!]$ is the stiffness tensor of the r^{th} phase. It is known that Eshelby tensor, $[\![S^{esh}]\!]$, and Hill concentration tensor, $[\![P]\!]$, are related by:

$$[\![S^{esh}]\!] = [\![P]\!] : [\![\mathrm{C}^{mat}]\!] \tag{4.20}$$

Using Eq. (4.20), Eq. (4.19) can be re-written as:

$$\boldsymbol{\varepsilon}^r(\mathbf{x}) = [[\![I]\!] + [\![P]\!] : ([\![\mathrm{C}^r]\!] - [\![\mathrm{C}^{mat}]\!])]^{-1} : \boldsymbol{E}^{\infty} \tag{4.21}$$

Now, using Eqs. (4.21) and (4.5), following relationship between $\boldsymbol{E}^{\infty}$ and $\boldsymbol{E}$ is obtained:

$$\boldsymbol{E}^{\infty} = < [[\![I]\!] + [\![P]\!] : ([\![\mathrm{C}^r]\!] - [\![\mathrm{C}^{mat}]\!])]^{-1} >_{\Omega}^{-1} : \boldsymbol{E} \tag{4.22}$$

Finally, by substituting (4.22) into (4.21), one can obtain the expression for $[\![\mathrm{A}^r]\!]$:

$$[\![\mathrm{A}^r]\!] = [[\![I]\!] + [\![P]\!] : ([\![\mathrm{C}^r]\!] - [\![\mathrm{C}^{mat}]\!])]^{-1} : < [[\![I]\!] + [\![P]\!] : ([\![\mathrm{C}^r]\!] - [\![\mathrm{C}^{mat}]\!])]^{-1} >_{\Omega}^{-1} \tag{4.23}$$

Now, by substituting Eq. (4.23) into Eq. (4.12) following expression for $[\![\mathrm{C}_{hom}]\!]$ is obtained:

$$[\![\mathrm{C}_{hom}]\!] = < [\![\mathrm{C}^r]\!] : [[\![I]\!] + [\![P]\!] : ([\![\mathrm{C}^r]\!] - [\![\mathrm{C}^{mat}]\!])]^{-1} >_{\Omega} : < [[\![I]\!] + [\![P]\!] : ([\![\mathrm{C}^r]\!] - [\![\mathrm{C}^{mat}]\!])]^{-1} >_{\Omega}^{-1} \tag{4.24}$$

Mori-Tanaka scheme (introduced by Mori and Tanaka 1973) and Self-consistent scheme (introduced by Hershey 1954, Kröner 1958, Budiansky 1965, and Hill 1965) are two effective medium theories that account for inclusion interactions through the use of Eshelby's solution in microelasticity. Mori-Tanaka scheme accounts for matrix-inclusion morphology, and Self-consistent scheme accounts for materials with random

microstructures in which none of the phases play the role of a matrix material. This method is known to be a good approximation for polycrystalline materials and composites with granular microstructures including shale (Ortega et al. 2007, Ulm and Abousleiman 2006, Bobko and Ulm 2008). In the Mori-Tanaka scheme one needs to set $[\![\mathrm{C}^{mat}]\!]$ in Eq. (4.24) equal to $[\![\mathrm{C}^{D}]\!]$, where $[\![\mathrm{C}^{D}]\!]$ denotes the stiffness tensor of the load bearing phase in the composite. On the other hand, in the self-consistent scheme one needs to set $[\![\mathrm{C}^{mat}]\!]$ in Eq. (4.24) equal to $[\![\mathrm{C}_{hom}]\!]$ which results in an implicit equation. This implies that none of the phases play a dominant role in the effective stiffness of the composite.

4.5 Hill Concentration Tensor ($[\![P]\!]$ Tensor)

To construct a model for heterogeneous materials one needs to evaluate Hill concentration tensor ($[\![P]\!]$ tensor). The role of Hill tensor is to capture orientation and morphology of inclusion phases considered for estimation of the overall strain concentration tensors.

The fourth-order Hill tensor reads [Zaoui 2002]:

$$[\![P]\!]_{ijkl} = -[\frac{\partial^2}{\partial x_j \partial x_k}(\int_{\Omega} G_{il}\,(\mathbf{x}-\mathbf{x}')\,dV\mathbf{x}')]_{(ij),(kl)} \tag{4.25}$$

where $G_{il}(\mathbf{x}-\mathbf{x}')$ represents the second-order Green's tensor that expresses the displacement at point $\mathbf{x}$ due to a unit force applied at a point $\mathbf{x}'$ in the medium. Laws and Dvorak (1987) expressed the generalized Hill concentration as follows:

$$[\![P]\!]_{ijkl} = \frac{1}{16\pi}(\mathcal{M}_{kijl} + \mathcal{M}_{kjil} + \mathcal{M}_{lijk} + \mathcal{M}_{ljik}) \tag{4.26}$$

where

$$\mathcal{M}_{kijl} = \int_{s(w)} \frac{a_1 a_2 a_3}{(a_1^2 w_1^2 + a_2^2 w_2^2 + a_3^2 w_3^2)^{\frac{3}{2}}} \Gamma_{kj}^{-1}(w) w_i w_l \, dS(w) \tag{4.27}$$

$\Gamma_{ik}(w) = C_{ijkl}^0 w_j w_l$ denotes the stiffness of the matrix; $dS(w)$ is the surface element of components w_1, w_2, w_3, and a_1, a_2, a_3 relate to the shape of ellipsoid. Evaluation of Eqs. (4.25) and (4.26) depends on the stiffness properties of the reference medium $[\![\mathrm{C}^{mat}]\!]$ and the shape and orientation of the inclusion phase [Ortega 2010]. Here, two different forms of Hill tensor are presented:

1- Spherical inclusions presented in an isotropic medium

2- Spherical inclusions presented in a transversely isotropic medium

It is to mention that many derivations of Hill tensor are available in literature for variations of stiffness property of $[\![\mathrm{C}^{mat}]\!]$ (reference medium) and the orientation and shape of the inclusion phase (see e.g. Mura 2013, and Withers 1989).

4.6 Spherical Inclusion in an Isotropic Medium

This case results in the simplest expression for the Hill tensor. It reads (see e.g. Dormieux et al. 2006):

$$[\![P]\!] = \frac{\alpha}{3K}[\![J]\!] + \frac{\beta}{2G}[\![K]\!] \tag{4.28}$$

where:

$$\alpha = \frac{3K}{3K+4G} \tag{4.29a}$$

$$\beta = \frac{6(K+2G)}{5(3K+4G)} \tag{4.29b}$$

K and G are the bulk and shear modulus of the isotropic medium, and $[\![J]\!]_{ijkl} = \frac{1}{3}(\delta_{ij}\delta_{kl})$ and $[\![K]\!]_{ijkl} = [\![I]\!]_{ijkl} - [\![J]\!]_{ijkl}$.

4.7 Spherical Inclusion in a Transversely Isotropic Medium

Evaluation of Christoffel matrix can be performed using the matrix operation shown below:

$$[\Gamma] = [w][C][w]^T \tag{4.30}$$

$[w]$ has a matrix form of [Ortega 2010]:

$$[\mathrm{w}] = \begin{pmatrix} w_1\ 0\ 0\ \frac{\sqrt{2}}{2}w_2\ 0\ \frac{\sqrt{2}}{2}w_3 \\ 0\ w_2\ 0\ \frac{\sqrt{2}}{2}w_1\ \frac{\sqrt{2}}{2}w_3\ 0 \\ 0\ 0\ w_3\ 0\ \frac{\sqrt{2}}{2}w_2\ \frac{\sqrt{2}}{2}w_1 \end{pmatrix} \tag{4.31}$$

where w is represented in spherical coordinates $0 < \theta < \pi$ and $0 < \Phi < 2\pi$ as following [Hellmich et al. 2004]:

$$\begin{aligned} w_1 &= sin\theta\ cos\Phi \\ w_2 &= sin\theta\ sin\Phi \\ w_3 &= cos\theta \end{aligned} \tag{4.32}$$

The non-zero terms in Eqs. (4.25) and (4.26) produce line integrals: ζ=$cos\theta$ and $d\zeta$=−$sin\theta d\theta$ that are evaluated numerically. For the final form of non-zero components of Hill tensor in Voigt's notation ($P_{11}, P_{12}, P_{13}, P_{33}, P_{44}$) see Ortega (2010), and Hellmich et al. (2004) among others.

4.8 Imperfect Interfaces

In this section, a set of formulations is introduced to obtain the effect of imperfect/weakened interface which plays an important role in the effective elasticity of mature organic rich shale, as mentioned in section 2.1.3. To this end, we introduce Interfacial Transition Zones (ITZs), and to calculate the effect of ITZ, generalized consistent model developed by Christensen and Lo (1979) is employed. This homogenization method, calculates the effective stiffness properties of a two-phase composite (ITZ and inclusion). In this approach, it is assumed that ITZ with a thickness of Δ_m covers the inclusion grain of a radius r_m. The formulas presented in Christensen and Lo (1979) for calculation of the effective properties are summarized below:

Eq. (4.33) calculated the bulk moduli of the homogenized *REV*, K^{em} as:

$$K^{em} = K^{itm} + \frac{f^e(K^m - K^{itm})(3K^{itm}+4G^{itm})}{3K^{itm}+4G^{itm}+3(1-f^e)(K^m-K^{itm})} \tag{4.33}$$

where f^e is the volume fraction of inclusion phase (e=equivalent inclusion in our case for mature organic rich shale) in the two-phase composite composed of the inclusion and ITZ. K^m, G^m, υ_m ($K^{itm}, G^{itm}, \upsilon_{itm}$) are bulk moduli, shear moduli and Poisson's ratio of equivalent inclusion (the ITZ), respectively. In order to obtain the shear moduli of the homogenized *REV*, one needs to solve the following parabolic equation:

$$A\left(\frac{G^{em}}{G^{itm}}\right)^2 + B\left(\frac{G^{em}}{G^{itm}}\right) + C = 0 \tag{4.34}$$

where G^{em} represents the shear moduli of the homogenized *REV*, and

$$A = 8\left(\frac{G^{em}}{G^{itm}} - 1\right)(4 - 5\upsilon_{itm})\eta_\alpha (f^e)^{\frac{10}{3}} - 2\left[63\left(\frac{G^{em}}{G^{itm}} - 1\right)\eta_\beta + 2\eta_\alpha\eta_\gamma\right](f^e)^{\frac{7}{3}} \tag{4.35a}$$

$$+252\left(\frac{G^{em}}{G^{itm}}-1\right)\eta_\beta(f^e)^{\frac{5}{3}}-25\left(\frac{G^{em}}{G^{itm}}-1\right)(7-12\upsilon_{itm}+8{\upsilon_{itm}}^2)\eta_\beta f^e$$

$$+4(7-10\upsilon_{itm})\eta_\beta\eta_\gamma$$

$$B=-4\left(\frac{G^{em}}{G^{itm}}-1\right)(1-5\upsilon_{itm})\eta_\alpha(f^e)^{\frac{10}{3}}+4\left[63\left(\frac{G^{em}}{G^{itm}}-1\right)\eta_\beta+2\eta_\alpha\eta_\gamma\right](f^e)^{\frac{7}{3}} \quad (4.35b)$$
$$-504\left(\frac{G^{em}}{G^{itm}}-1\right)\eta_\beta(f^e)^{\frac{5}{3}}+150\left(\frac{G^{em}}{G^{itm}}-1\right)(3-\upsilon_{itm})\upsilon_{itm}\eta_\beta f^e$$

$$+3(15\upsilon_{itm}-7)\eta_\beta\eta_\gamma$$

$$C=4\left(\frac{G^{m}}{G^{itm}}-1\right)(5\upsilon_{itm}-7)\eta_\alpha(f^e)^{\frac{10}{3}}-2\left[63\left(\frac{G^{em}}{G^{itm}}-1\right)\eta_\beta+2\eta_\alpha\eta_\gamma\right](f^e)^{\frac{7}{3}} \quad (4.35c)$$
$$+252\left(\frac{G^{em}}{G^{itm}}-1\right)\eta_\beta(f^e)^{\frac{5}{3}}+25\left(\frac{G^{em}}{G^{itm}}-1\right)({\upsilon_{itm}}^2-7)\eta_\beta f^e(5\upsilon_{itm}+7)\eta_\beta\eta_\gamma$$

With

$$\eta_\alpha=\left(\frac{G^{m}}{G^{itm}}-1\right)(49-50\upsilon_m\upsilon_{itm})+35\left(\frac{G^{m}}{G^{itm}}\right)(\upsilon_m-2\upsilon_{itm})+35(2\upsilon_m-\upsilon_{itm}) \quad (4.35d)$$

$$\eta_\beta=5\upsilon_m\left(\frac{G^{m}}{G^{itm}}-8\right)+7\left(G^m+G^{itm}+4\right) \quad (4.35e)$$

$$\eta_\gamma=\frac{G^{m}}{G^{itm}}(8-10\upsilon_{itm})+(7-5\upsilon_{itm}) \quad (4.35f)$$

$$\phi_m=\left(\frac{r_m}{r_m+\Delta_m}\right)^3 \quad (4.35g)$$

4.9 Chapter Summary

Chapter 4 stablishes a basis of micropromechanics which can be used in order to obtain the homogenized/effective poroelastic response of a composite material, under the assumption of linear microporoelasticity. It is started with introducing *REV* and scale separability conditions, which define the constraints under which tools of continuum mechanics can be applied. Next, through a framework of inclusion-based effective medium theories, it estimates the effective response of a composite material, and

elaborates on the estimation of important constituent of this framework, such as Hill concentration tensor. Finally, a generalized self-consistent model is introduced in order to model and estimate the effect of weakened/imperfect interfaces.

5 MULTISCALE MODEL FOR MATURE ORGANIC-RICH SHALE

The objective of this chapter is to integrate the developments presented in previous chapter into multiscale thought model of mature organic-rich shales. To this end, first, the volume fractions of considered phases at each length scale are introduced. Then, formulations to capture the effective anisotropic poroelasticity at each length scale are derived. Ultimately, the undrained behavior of mature organic-rich shales is obtained based on their drained behavior.

5.1 Volume Fractions

Based on the structural thought model developed in chapter 2, following volume fractions are introduced. Note that mature organic-rich shales exhibit a granular system (Monfared and Ulm 2016, Abedi et al. 2016b), which qualifies the use of self-consistent scheme for homogenization at different scales. Because of self-consistent texture, it is assumed that an evenly distributed porosity exists in all phases of the material. At level II, volume fractions read:

$$f^{clay} + f^{kerogen} + f^{inc} + \phi^{\mathrm{II}} = 1 \tag{5.1}$$

where

$$f^{inc} = (1 - \phi^{\mathrm{II}}) \frac{\sum_{i=1}^{N} \frac{m_i}{\rho_i}}{\sum_{j=1}^{P} \frac{m_j}{\rho_j}} \tag{5.2a}$$

m_k and ρ_k are the mass percent and grain density of k^{th} phase, P stands for all the organic and inorganic phases, and N denotes all non-clay inorganic constituents. Also, volume fraction of clay and kerogen is defined as:

$$f^r = (1-\phi^{\mathrm{II}})\frac{\frac{m_r}{\rho_r}}{\sum_{j=1}^{P}\frac{m_j}{\rho_j}} \ (r = clay, kerogen) \tag{5.2b}$$

It is assumed that $f^{inc} = f^{calcite} + f^{quartz}$ where $f^{calcite}$ and f^{quartz} denote the volume fractions of calcite and quartz at level II, respectively. At level I, volume fractions satisfy following constraint:

$$\eta^{clay} + \eta^{kerogen} + \varphi^{\mathrm{I}} = 1 \tag{5.3}$$

where

$$\eta^r = \frac{f^r}{f^{clay}+f^{kerogen}+\phi^{\mathrm{II}}_{k+c}} \ (r = clay, kerogen) \tag{5.4a}$$

where ϕ^{II}_{k+c} denotes the portion of porosity at level II, ϕ^{II}, which belongs to clay and kerogen phases:

$$\phi^{\mathrm{II}}_{k+c} = \phi^{\mathrm{II}}\ \frac{f^{clay}+f^{kerogen}}{f^{clay}+f^{kerogen}+f^{inc}} \tag{5.4b}$$

and

$$\varphi^{\mathrm{I}} = \frac{\phi^{\mathrm{II}}_{k+c}}{f^{clay}+f^{kerogen}+\phi^{\mathrm{II}}_{k+c}} \tag{5.4c}$$

also, φ^{I} is divided between clay and kerogen proportional to their volume fractions:

$$\varphi^{\mathrm{clay}} = \frac{\eta^{clay}}{\eta^{clay}+\eta^{kerogen}}\ \varphi^{\mathrm{I}} \tag{5.4d}$$

$$\varphi^{\mathrm{kerogen}} = \frac{\eta^{kerogen}}{\eta^{clay}+\eta^{kerogen}}\ \varphi^{\mathrm{I}} \tag{5.4e}$$

To obtain effective stiffness tensor of porous inclusions with ITZ, a three-step homogenization is performed. The first step homogenization is needed to obtain the effective elasticity tensor of solid matrix, i.e. a self-consistent mixture of quartz and calcite. The second step of homogenization is performed through generalized self-consistent method to introduce the weakened interface through ITZ. Finally, third self-consistent homogenization is needed to introduce porosity to the composite of calcite and quartz with a weakened interface. The obtained stiffness tensor of weakened porous inclusion is then utilized for calculation of effective stiffness tensor at level II. Volume fractions needed for the three-step homogenization scheme are:

- Step one: $f_{inc}^{m,1} = \frac{f^m}{f^{quartz}+f^{calcite}}$ (m =quartz, calcite) (5.5a)
- Step two: $f_{inc}^{,2} = (\frac{2-\Delta_{itz}}{2})^3$ and $f_{itz}^{,2} = 1-(\frac{2-\Delta_{itz}}{2})^3$ (5.5b)
- Step three: $f_{inc}^{,3} = \frac{f^{inc}}{f^{inc}+\phi^{inc}}$; $\phi_{inc}^{,3} = 1-f_{inc}^{,3}$ ($\phi^{inc} = \phi^{\mathrm{II}} - \phi_{k+c}^{\mathrm{II}}$) (5.5c)

In Eq. (5.5b) Δ_{itz} (μm) denotes the thickness of ITZ. It is assumed that ITZ demonstrates a homogeneous behavior and the average sum of radius of inclusion grain and thickness of ITZ is chosen to be $2\mu m$ [Monfared and Ulm (2016)].

5.2 Level I

At level I, there are two porous phases considered in our model: homogenized porous clay and homogenized porous kerogen. Behavior of each of these porous composites can be described through employing the classical poroelastic state equations [Coussy 2004]:

$$\boldsymbol{\Sigma} = [\![\mathrm{C}_{hom}]\!] : \boldsymbol{E} - [\alpha]p \tag{5.6a}$$

$$\varphi - \varphi_0 = [\alpha] : \boldsymbol{E} + \frac{p}{N} \tag{5.6b}$$

Where

$\boldsymbol{\Sigma}$: Stress average ($\boldsymbol{\Sigma} = < \boldsymbol{\sigma}(\mathbf{x}) >_{\Omega}$)

$\boldsymbol{E}$: Strain average ($\boldsymbol{E} = < \boldsymbol{\varepsilon}(\mathbf{x}) >_{\Omega}$)

p: Pore pressure

$\varphi - \varphi_0$: Lagrangian porosity change

$[\![\mathrm{C}_{hom}]\!]$: Homogenized stiffness tensor

$[\alpha]$: matrix of Biot pore pressure coefficients

N: Solid Biot modulus

Equations above describe the poroelastic behavior of a *REV* with domain Ω. Ω consists of the solid domain (clay or kerogen) $\Omega^s = (1 - \varphi_0)\Omega$ and the pore space $\Omega^p = \varphi_0\Omega$, where $\varphi_0 = \frac{\varphi^{\mathrm{clay}}}{[\varphi^{\mathrm{clay}} + \eta^{clay}]} = \frac{\varphi^{\mathrm{kerogen}}}{[\varphi^{\mathrm{kerogen}} + \eta^{kerogen}]}$.

Using a description of the stress field in the *REV*:

$$\boldsymbol{\sigma}(x) = [\![C(\mathbf{x})]\!] : \boldsymbol{\varepsilon}(\mathbf{x}) + \boldsymbol{\sigma}^T(\mathbf{x}) \qquad (\mathbf{x} \in \Omega) \tag{5.7}$$

with the following distribution of elastic properties and eigenstresses:

$$\mathbb{C}(\mathbf{x}) = \begin{cases} 0 & (\mathbf{x} \in \Omega^p) \\ [\![C^s]\!] & (\mathbf{x} \in \Omega^s) \end{cases} \tag{5.8a}$$

$$\boldsymbol{\sigma}^T(x) = \begin{cases} -p[1] & (x \in \Omega^p) \\ 0 & (x \in \Omega^s) \end{cases} \tag{5.8b}$$

where [1] denotes second order identity tensor. Then, the mechanics problem of finding microscopic stress and strain when *REV* is subjected to the macroscopic strain $\boldsymbol{E}$ and microscopic eigenstress $\boldsymbol{\sigma}^T$ is associated with the following equations:

$$\nabla.\boldsymbol{\sigma} = 0 \qquad (\mathbf{x} \in \Omega)$$

$$\boldsymbol{\sigma} = [\![C(\mathbf{x})]\!]:\boldsymbol{\varepsilon} + \boldsymbol{\sigma}^T(\mathbf{x}) \qquad (\mathbf{x} \in \Omega) \tag{5.9}$$

$$\xi = \boldsymbol{E}.\mathbf{x} \qquad (\mathbf{x} \in \Omega)$$

One can separate the above problem into two problems, each with one of the loading conditions ($\boldsymbol{\sigma}^T, \boldsymbol{E}$), since the defined problem is linear:

1- Problem corresponds to the response of *REV* to the $\boldsymbol{E}$ while $\boldsymbol{\sigma}^T$ is zero.

2- Problem corresponds to the response of *REV* to the $\boldsymbol{\sigma}^T$ while $\boldsymbol{E}$ is zero.

The final solution of the microscopic stress and strain fields is the superposition of stress and strains fields of each sub-problem defined above.

Solution of sub-problem 1:

The problem of *REV* subjected only to the $\boldsymbol{E}$ is associated with the following equations:

$$\nabla.\boldsymbol{\sigma}^1 = 0 \qquad (\mathrm{x} \in \Omega)$$

$$\boldsymbol{\sigma}^1 = [\![C(\mathbf{x})]\!]:\boldsymbol{\varepsilon}^1 \quad (\mathrm{x} \in \Omega) \tag{5.10}$$

$$\xi^1 = \boldsymbol{E}.\mathbf{x} \qquad (\mathbf{x} \in \partial\Omega)$$

Using (4.9b):

$$\varepsilon^1(\mathbf{x}) = [\![A(\mathbf{x})]\!]:\boldsymbol{E} \tag{5.11}$$

Using Eqs. (5.11), (5.8), and (5.7):

$$\boldsymbol{\Sigma}^1 = <\boldsymbol{\sigma}^1(\mathbf{x})>_\Omega = <[\![C(\mathbf{x})]\!]:[\![A(\mathbf{x})]\!]>_\Omega : \boldsymbol{E} \tag{5.12}$$

Thus, the drained homogenized stiffness tensor is equal to:

$$[\![\mathrm{C}_{hom}]\!] := < [\![C(\mathbf{x})]\!] : [\![A(\mathbf{x})]\!] >_{\Omega} = \eta^{s} [\![C^{s}]\!] : [\![A^{s}]\!] \tag{5.13}$$

where

$$[\![A^{s}]\!] = [[\![I]\!] + [\![P^{sc}]\!] : ([\![C^{s}]\!] - [\![\mathrm{C}_{hom}]\!])]^{-1} : < [[\![I]\!] + [\![P^{sc}]\!] : ([\![C^{s}]\!] - [\![\mathrm{C}_{hom}]\!])]^{-1} >_{\Omega}^{-1} \tag{5.14}$$

$\{s = clay, kerogen\}$

where $[\![P^{sc}]\!]$ represents Hill polarization tensor obtained from a self-consistent approach.

Solution of sub-problem 2:

The problem of *REV* subjected to the $\boldsymbol{\sigma}^{T}$ is associated with the following equations:

$$\begin{aligned} &\nabla . \boldsymbol{\sigma}^{2} = 0 && (x \in \Omega) \\ &\boldsymbol{\sigma}^{2} = [\![C(\mathbf{x})]\!] : \boldsymbol{\varepsilon}^{2} + \boldsymbol{\sigma}^{T}(x) && (x \in \Omega) \\ &\xi^{2} = 0 && (x \in \partial\Omega) \end{aligned} \tag{5.15}$$

In this case the macroscopic stress $\boldsymbol{\Sigma}^{2}$ equals the average of microscopic stress $\boldsymbol{\sigma}^{2}$over the *REV* volume. Also, using the Hill lemma to the $\boldsymbol{\sigma}^{2}$ and $\boldsymbol{\varepsilon}^{1}$ one obtains:

$$< \boldsymbol{\sigma}^{2} : \boldsymbol{\varepsilon}^{1} >_{\Omega} = \boldsymbol{\Sigma}^{2} : \boldsymbol{E} \tag{5.16}$$

Using (5.15) and (5.16), one obtains:

$$< \boldsymbol{\sigma}^{2} : \boldsymbol{\varepsilon}^{1} >_{\Omega} = < \boldsymbol{\varepsilon}^{2} : [\![C(\mathbf{x})]\!] : \boldsymbol{\varepsilon}^{1} >_{\Omega} + < \boldsymbol{\sigma}^{T}(\mathbf{x}) : \boldsymbol{\varepsilon}^{1} >_{\Omega} \tag{5.17}$$

Second use of hill Lemma to the $\boldsymbol{\varepsilon}^{2}$ and $\boldsymbol{\sigma}^{1}$ yields (for this load case $< \boldsymbol{\varepsilon}^{2} >_{\Omega} = 0$)

$$< \boldsymbol{\varepsilon}^{2} : [\![C(\mathbf{x})]\!] : \boldsymbol{\varepsilon}^{1} >_{\Omega} = 0 \tag{5.18}$$

Using (5.18), (5.17), and (5.11):

$$\boldsymbol{\Sigma}^{2} = < \boldsymbol{\sigma}^{T}(x) : [\![A(\mathbf{x})]\!] >_{\Omega} \tag{5.19}$$

The above equation is known as Levin's theorem (Dormieux et. al 2006, and Zaoui 2002). $\boldsymbol{\Sigma}^{2}$ is the variation in pressure under no macroscopic strain. Using Eqs. (5.19) and (5.8a):

$$\boldsymbol{\Sigma}^2 = \boldsymbol{\Sigma}^T = -p\varphi_0[1]:[\![A_p]\!] \tag{5.20}$$

where $[\![A_p]\!]$ is the strain localization tensor associated with the pore inclusions. One can calculate the matrix of Biot pore pressure coefficients, $[\alpha]$, by comparing the $\boldsymbol{\sigma}^T$ and $\boldsymbol{\Sigma}^T$:

$$[\alpha] = \varphi_0[1]:[\![A_p]\!] = (1-\eta^s)[1]:[\![A_p]\!] \tag{5.21}$$

Now, superposition of macroscopic stresses of both load cases yields the Eq. (5.6a). Now, we want to derive an expression for the strain field in the pore space as a function of p (pore pressure) for the second sub-problem:

We know that $< \boldsymbol{\varepsilon}^2 >_{\Omega} = 0$, thus:

$$\varphi_0 < \boldsymbol{\varepsilon}^2 >_{\Omega^p} = -(1-\varphi_0) < \boldsymbol{\varepsilon}^2 >_{\Omega^s} \tag{5.22}$$

Now, only considering solid domain:

$$(1-\varphi_0) < \boldsymbol{\varepsilon}^2 >_{\Omega^s} = (1-\varphi_0)[\![S^s]\!]: < \boldsymbol{\sigma}^2 >_{\Omega^s} \tag{5.23}$$

Also, we have:

$$\boldsymbol{\Sigma}^2 = < \boldsymbol{\sigma}^2 >_{\Omega} = -p[\alpha]$$

$$< \boldsymbol{\sigma}^2 >_{\Omega^p} = -p[1] \tag{5.24}$$

$$< \boldsymbol{\sigma}^2 >_{\Omega} = < \boldsymbol{\sigma}^2 >_{\Omega^p} + < \boldsymbol{\sigma}^2 >_{\Omega^s}$$

Using above three equations, one can obtain:

$$(1-\varphi_0) < \boldsymbol{\sigma}^2 >_{\Omega^s} = (\varphi_0[1] - [\alpha]) \tag{5.25}$$

By using (5.25) in (5.22) and (5.23), we get:

$$\varphi_0[1] : < \boldsymbol{\varepsilon}^2 >_{\Omega^p} = p[1]:[\![S^s]\!]:([\alpha] - \varphi_0[1]) \tag{5.26}$$

The strain field solution of Eq. (5.9) is the superposition of two sub-problems, namely $\boldsymbol{\varepsilon}^1$ and $\boldsymbol{\varepsilon}^2$. The second one is derived above. For the solution to the first sub-problem we use Eqs. (5.11) and (5.21):

$$\varphi_0[1]: < \boldsymbol{\varepsilon}^2 >_{\Omega^p} = \varphi_0[1]: [\![A_p]\!]: \boldsymbol{E} = [\alpha]: \boldsymbol{E} \tag{5.27}$$

Finally, by the superposition of the results of (5.26) and (5.27) one can obtain the total change in porosity (Eq. 5.6b).

In Eq. (5.6b) the solid Biot modulus is defined as:

$$\frac{1}{N} = [1]: \mathbb{S}^s: ([\alpha] - \varphi_0[1]) = \mathbf{1}: [\![S^s]\!]: ([\alpha] - (1 - \eta^s)[1]) \tag{5.28}$$

Performing the steps mentioned above, following poroelastic coefficients and homogenized properties for porous clay and porous kerogen at level I are obtained:

$Porous\ Clay\ (pc)$

$$[\![\mathrm{C}_{hom}]\!]_{pc} = (1 - \varphi_0)[\![C^{clay}]\!]: [\![A^{clay}]\!] \tag{5.29a}$$

$$[\alpha]^{pc} = \varphi_0[1]: [\![A^{p-clay}]\!] \tag{5.29b}$$

$$\frac{1}{N^{pc}} = [1]: [\![S^{clay}]\!]: ([\alpha]^{pc} - \varphi_0[1]) \tag{5.29c}$$

$Porous\ Kerogen\ (pk)$

$$[\![\mathrm{C}_{hom}]\!]_{pk} = (1 - \varphi_0)[\![C^{kerogen}]\!]: [\![A^{kerogen}]\!] \tag{5.30a}$$

$$[\alpha]^{pk} = \varphi_0[1]: [\![A^{p-kerogen}]\!] \tag{5.30b}$$

$$\frac{1}{N^{pk}} = [1]: [\![S^{kerogen}]\!]: ([\alpha]^{pk} - \varphi_0[1]) \tag{5.30c}$$

where $\varphi_0 = \varphi^{\mathrm{I}} = \phi^{\mathrm{II}}$ due to the self ocnsitent texture of mature organic-rich shale.

To obtain the homogenized stiffness tensor and poroelastic coefficients at level I, following formulations are employed:

$Homogenized\ level\ I$

$$[\![C^I_{hom}]\!] = < [\![\mathrm{C}]\!]: [\![A(\mathbf{x})]\!] >_{\Omega^{\mathrm{I}}} = (\varphi^{clay} + \eta^{clay})[\![\mathrm{C}_{hom}]\!]_{pc}: [\![A^{pc}]\!] \tag{5.31a}$$

$$+(\varphi^{kerogen} + \eta^{kerogen})[\![\mathrm{C}_{hom}]\!]_{pk}: [\![A^{pk}]\!]$$

$$[\alpha]^{I,hom} = (\varphi^{clay} + \eta^{clay})[\alpha]^{pc} + (\varphi^{kerogen} + \eta^{kerogen})[\alpha]^{pk} \tag{5.31b}$$

$$\frac{1}{N^I} = (\varphi^{clay} + \eta^{clay})\frac{1}{N^{pc}} + (\varphi^{kerogen} + \eta^{kerogen})\frac{1}{N^{pk}} \tag{5.31c}$$

5.3 Level II

At this level shale is considered as a composite consisting of porous equivalent inclusion grains (porosity + inclusions + ITZs) and a porous solid fabric upscaled from level I. Thus, continuous stress field in the REV at this scale reads:

$$\boldsymbol{\sigma}(x) = [\![\mathrm{C}(\mathbf{x})]\!] : \boldsymbol{\varepsilon}(\mathbf{x}) + \boldsymbol{\sigma}^{T}(\mathbf{x}) \qquad (\mathbf{x} \in \Omega) \tag{5.32}$$

where

$$[\![\mathrm{C}(\mathbf{x})]\!] = \begin{cases} [\![C_{hom}^{I}]\!] & (\mathbf{x} \in \Omega_1^{hom}) \\ [\![C_{hom}^{por-einc}]\!] & (\mathbf{x} \in \Omega^{por-einc}) \end{cases} \tag{5.33a}$$

$$\boldsymbol{\sigma}^{T}(x) = \begin{cases} -[\alpha]^{\boldsymbol{I}} p & (x \in \Omega_1^{hom}) \\ -[\alpha]^{\boldsymbol{por-einc}} p & (x \in \Omega^{epor-inc}) \end{cases} \tag{5.33b}$$

$[\![C_{hom}^{por-einc}]\!]$ represents stiffness tensor associated with the porous equivalent inclusion grains, and $[\alpha]^{\boldsymbol{por-einc}}$ denotes the tensor of Biot pore pressure coefficient of the porous equivalent inclusion.

For the homogenized $[\alpha]^{\boldsymbol{II}}$ (homogenized Biot pore pressure at level II), the sub-problem associated with the response of a *REV* to a prescribed macroscopic strain field at the boundaries while $\boldsymbol{\sigma}^{T} = 0$ is considered (sub-problem 1 at level I). Considering strain compatibility condition and the second poroelastic state equation, one can obtain:

$$(\varphi - \varphi_0)^1 = < [\alpha]^{\boldsymbol{I}} \varepsilon^1 > = \sum_{r=1}^{n} \eta^r ([\alpha]^{\boldsymbol{I}})^r \, (\varepsilon^r)^1 = \sum_{r=1}^{n} \eta^r ([\alpha]^{\boldsymbol{I}})^r [\![A^r]\!] : \boldsymbol{E} = [\alpha]^{I,hom} : \boldsymbol{E} \tag{5.34}$$

From (5.34) it can be deduced that:

$$[\alpha]^{hom} = < [\alpha]^r : [\![A^r]\!] >_{\Omega^s} \tag{5.35}$$

and r denoted the solid phases.

In order to compute Biot solid modulus, one needs to consider sub-problem 2 from Level I, where response of a *REV* to the eigenstresses in the pore space is studied while $\boldsymbol{E}$ is zero. We have:

$$(\varphi - \varphi_0)^2 = < \frac{p}{N^I} >_{\Omega^s} = \frac{p}{N^I} \tag{5.36}$$

Hence:

$$\frac{1}{N^{hom}} = < \frac{1}{N^r} >_{\Omega^s} \tag{5.37}$$

Adapting Eq. (5.28) for the porous equivalent inclusion, we get:

$$\frac{1}{N^{por-einc}} = [1] : f_{inc}^{,3} \left([\![S^{e-inc}]\!] \right) : ([1] : ([\![I]\!] - [\![A^{e-inc}]\!])) \tag{5.38}$$

Now, one can write the homogenized drained stiffness tensor as:

$$[\![C_{hom}^{II}]\!] = < [\![\mathrm{C}]\!] : [\![A(\mathbf{x})]\!] >_{\Omega^{\mathrm{II}}} = \left(f^{por-einc} \right) [\![C_{hom}^{por-einc}]\!] : [\![A^{por-einc}]\!] + \left(1 - f^{por-einc} \right) [\![C_{hom}^{I}]\!] : [\![A^{hom,I}]\!] \tag{5.39}$$

$$f^{por-einc} = \phi^{inc} + f^{inc} \tag{5.40}$$

Poroelastic coefficients associated with the upscaled level I read:

$$[\alpha]_I^{\mathrm{up}} = [\alpha]^I : ([\![I]\!] - f^{por-einc} [\![A^{por-einc}]\!]) \tag{5.41}$$

$$\frac{1}{N_I^{\mathrm{up}}} = \frac{1 - f^{por-einc}}{N^I} + [\alpha]^I : \left([\![C_{hom}^I]\!] - [\![C_{hom}^{por-einc}]\!] \right)^{-1} : \left(-[\alpha]_I^{\mathrm{up}} + (1 - f^{por-einc}) [\alpha]^I \right) \tag{5.42}$$

Effective $[\alpha]^{II}$ and N^{II} read:

$$[\alpha]^{II} = f^{por-einc} [\alpha]^{por-einc} + (1 - f^{por-einc}) \, [\alpha]_I^{\mathrm{up}} \tag{5.43}$$

$$\frac{1}{N^{II}} = f^{por-einc} \frac{1}{N^{por-einc}} + (1 - f^{por-einc}) \frac{1}{N_I^{\mathrm{up}}} \tag{5.44}$$

5.4 Undrained Behavior

In this section, we aim to derive expressions for undrained stiffness properties of shales when pores are fully saturated. The Lagrangian fluid mass content for a fully saturated pore system reads:

$$m = \varphi \rho^{fl}(P) \tag{5.45}$$

The change in fluid density due to applying pressure can be characterized by the following equation: (Coussy 2004):

$$\frac{\rho^{fl}}{\rho^{fl,0}} = 1 + \frac{P}{K^{fl}} \tag{5.46}$$

where $\rho^{fl,0}$ is the initial fluid density, and K^{fl} is bulk moduli of fluid. Using Eqs. (5.6a), (5.6b), and (5.42) one can write:

$$\boldsymbol{\Sigma} = [\![C_{hom}^{J,un}]\!] : (\boldsymbol{E} - \boldsymbol{B}^J \frac{(m-m0)^J}{\rho^{fl,0}}) \tag{5.47a}$$

$$\frac{(m-m0)^J}{\rho^{fl,0}} = [\alpha]^J : \boldsymbol{E} + \frac{p}{M^J} \tag{5.47b}$$

where:

J: indicates the level ; $J = I,\ II$

M^J: overall Biot modulus ; $\frac{1}{M^J} = \frac{1}{N^J} + \frac{{\phi_0}^J}{K^{fl}}$

$\boldsymbol{B}^J$: second-order tensor of Skempton coefficients ; $\boldsymbol{B}^J = M^J\ [\![S_{hom}^{J,un}]\!] : [\boldsymbol{\alpha}]^J$

$(\mathbb{C}_{\mathrm{hom}})^{J,un}$**:** undrained stiffness tensor ; $[\![C_{hom}^{J,un}]\!] = [\![C_{hom}^{J}]\!] + (M[\boldsymbol{\alpha}]\otimes[\boldsymbol{\alpha}])^J$

And:

${\phi_0}^I = \varphi^{\mathrm{I}}$ at level $J=I$, and ${\phi_0}^{II}=\phi^{\mathrm{II}}$ at level $J=II$.

Biot solid modulus, *N*, characterizes pore volume changes due to variations in pore pressure under the condition of $\boldsymbol{E} = 0$; tensor of Biot pore pressure coefficients, $[\alpha]$, is a correction factor for stress in solid frame due to pore pressure variations [Cheng 1997, Rice and Cleary 1976]; tensor of Skempton pore pressure coefficients, $\boldsymbol{B}$, indicates pore pressure variations as a result of stress application [Skempton 1984].

5.5 Chapter Summary

This chapter develops a predictive multiscale model for poroelastic properties of mature organic-rich shale based on the developments of chapter 4, which takes into account the structure and morphology of these shales. First, the volume fractions of considered phases at multiple length scales are calculated. It is assumed that mature organic-rich shales exhibit a self-consistent texture, and consequently the distribution of porosity between all phases at different length scales is even. Then microporoelastic properties of shale at two levels (level I and level II) are obtained by considering two scenarios:

1- Problem corresponds to the response of *REV* to the $\boldsymbol{E}$ while $\boldsymbol{\sigma}^T$ is zero.

2- Problem corresponds to the response of *REV* to the $\boldsymbol{\sigma}^T$ while $\boldsymbol{E}$ is zero.

The superposition of these scenarios returns the final answer. Finally, undrained properties of shales are obtained by integrating classical poroelastic state equations and drained properties of shales.

6 PROBABILISTIC DEVELOPMENTS

So far, the deterministic multiscale model is developed assuming that all the reported values of input parameters to the model, i.e. volume fractions, stiffness tensors, etc., are the same as their true values in the samples. What if this assumption is not correct? Based on a literature survey it is deduced that almost all the input parameters which are obtained by carrying some experiments are not accurate, and there are some fluctuations in their values based on different experiments. The extreme case is the stiffness values of clay minerals. Thus, it is a useful practice to try to consider the uncertainty in input parameters of the model, and estimate the result of propagating these uncertainties in multiple levels to have a more robust and reliable model. To this end, in the following sections, probabilistic models to capture the uncertainty in two separate types of input parameters are presented:

- Fourth-order tensor of stiffness of materials (e.g. clay) belonging to the TI class of symmetry
- Scalar parameters (e.g. volume fractions in the model, bulk moduli and Poisson's ratio of kerogen, thickness of the ITZ, etc.)

6.1 Notations

Below is the set of notations that will be used throughout section 6:

- Superscript or subscript "ti" refers to "transversely isotropic"

- $\mathbb{E}\mathrm{la}^{\mathrm{ti}}$ is the set of all the fourth-order elasticity tensors that display transversely isotropic material symmetry
- $[\![C]\!]$ is deterministic fourth-order elasticity tensor ($[\![\boldsymbol{C}]\!]$ for stochastic)
- $[C]$ is deterministic second-order elasticity tensor which is the matrix representation of the elasticity tensor ($[\boldsymbol{C}]$ for stochastic)
- Deterministic vectors and scalars are denoted by $\boldsymbol{a}$ and a ($\boldsymbol{A}$ and A for stochastic, respectively)
- $\mathbb{M}_6(\mathbb{R})$ is the set of real (6x6) matrices.

6.2 Probabilistic Developments of a Fourth-Order Stiffness Tensor Belonging to the TI Class of Symmetry (i.e. Clay Stiffness Tensor)

In this section, we aim to develop the probability distribution of stochastic elasticity tensors of organic-rich shales at level 0, i.e. the elasticity tensor of consolidated clay. To this end, we assume that the elasticity tensor of consolidated clay at level 0 for all different organic-rich shales belongs to the class of transversely isotropic materials, $[\![C^{\mathrm{ti}}]\!]$, which has five independent components, namely C_{1111}, C_{1122}, C_{1133}, C_{3333}, C_{2323}.

It is being shown that any element in $[\![C^{\mathrm{ti}}]\!]$ can be decomposed as:

$$[\![C^{\mathrm{ti}}]\!] = \sum_{i=1}^{5} c_i [\![E_{\mathrm{ti}}^{(i)}]\!], \tag{6.1}$$

Where $\left\{[\![E_{\mathrm{ti}}^{(i)}]\!]\right\}_{i=1}^{5}$ is a tensor basis of $\mathbb{E}\mathrm{la}^{\mathrm{ti}}$, and $\{c_i\}_{i=1}^{5}$ are coefficients that must satisfy some properties related to the positiveness of $[\![C^{\mathrm{ti}}]\!]$ [Guilleminot and Soize 2013a].

It is possible to decompose a random elasticity tensor, $[\![\mathbf{C}^{\mathrm{ti}}]\!]$, with values in $\mathbb{E}\mathrm{la}^{\mathrm{ti}}$ by extending Eq. (6.1) as:

$$[\![\mathbf{C}^{\mathrm{ti}}]\!] = \sum_{i=1}^{5} C_i [\![E_{\mathrm{ti}}^{(i)}]\!], \tag{6.2}$$

where $\{C_i\}_{i=1}^{5}$ now play the role of random variables and $\left\{[\![E_{\mathrm{ti}}^{(i)}]\!]\right\}_{i=1}^{5}$ is a determinist basis for $\mathbb{E}\mathrm{la}^{ti}$.

As stated before, the goal of this section is to develop the probability distribution of stochastic elasticity tensor of consolidated clay. To this end, we introduce stochastic elasticity matrix $[\mathbf{C}_{clay}^{ti}]$, which is the matrix representation of stochastic consolidated clay elasticity tensor, which can be modeled as a $\mathbb{M}_6^{ti}(\mathbb{R})$-valued random variable [Guilleminot and Soize 2013a]:

$$[\mathbf{C}_{clay}^{ti}] = \sum_{i=1}^{5} C_i^{clay} \left[E_{\mathrm{ti}}^{(i)}\right] \tag{6.3}$$

where $\left\{\left[E_{\mathrm{ti}}^{(i)}\right]\right\}_{i=1}^{5}$ are the matrix representations of the deterministic basis tensor $\left\{[\![E_{\mathrm{ti}}^{(i)}]\!]\right\}_{i=1}^{5}$.

In this thesis, Walpole's basis tensors are utilized as the basis for transversely isotropic class of symmetry [Walpole 1984].

For self-readability, we recall the Walpole's basis tensors for the symmetry class of transversely isotropic:

Let matrix representation of stochastic consolidated clay elasticity matrix, $[\mathbf{C}_{clay}^{ti}]$, decomposed as:

$$[\mathbf{C}_{clay}^{ti}] = C_1^{clay}[E^{(1)}] + C_2^{clay}[E^{(2)}] + C_3^{clay}[E^{(3)}] + C_4^{clay}[E^{(4)}] + C_5^{clay}[E^{(5)}] \tag{6.4}$$

where $\{[E^{(i)}]\}_{i=1}^{5}$ are matrix representation of the fourth-order tensors defined as [Guilleminot and Soize 2013a]:

$[\![E^{(1)}]\!] = [m]\otimes[m]$, $[\![E^{(2)}]\!] = \frac{1}{2}[h]\otimes[h]$, $[\![E^{(3)}]\!] = \frac{1}{\sqrt{2}}[m]\otimes[h] + \frac{1}{\sqrt{2}}[h]\otimes[m]$, $[\![E^{(4)}]\!] = [h]\odot[h] - [\![E^{(2)}]\!]$, and $[\![E^{(5)}]\!] = [\![\mathbb{I}]\!] - [\![E^{(2)}]\!] - [\![E^{(2)}]\!] - [\![E^{(4)}]\!]$.

where $[h]$ and $[m]$ are second-order symmetric tensors defined as:

$[m]= \boldsymbol{n}\otimes\boldsymbol{n}$ and $[h]= [I] - [m]$, where $\boldsymbol{n}$ denotes the unit normal orthogonal to the plane of isotropy, $[I]$ is the second-order symmetry identity tensor and $\odot$ is the usual symmetrized tensor product ($\odot$ is defined by: $2([X]\odot[Y])_{ijkl} = [X]_{ik}[Y]_{jl} + [X]_{il}[Y]_{jk}$, where $[X]$ and $[Y]$ are second-order tensors).

Considering Eq. (6.2) (or (6.3)) one can deduce that constructing a probabilistic model for $\{C_i^{clay}\}_{i=1}^{5}$ is the same as construction of a probabilistic model for $[\mathbf{C}_{clay}^{ti}]$ (or random elasticity tensor $[\![\mathbf{C}_{clay}^{ti}]\!]$). In the following the steps taken for constructing a probabilistic model for random coordinates $\{C_i^{clay}\}_{i=1}^{5}$ are addressed.

6.2.1 Model Developments

"Uncertainty propagation is often based on strong assumptions regarding the probability distributions, which are mostly chosen for the sake of theoretical and numerical convenience rather than deduced from a probabilistic reasoning" [Guilleminot and Soize 2013a]. Hence, such models are not reliable. To circumvent this issue and increase the reliability of constructing a probabilistic model for the random coordinates, theory of random matrices and Maximum Entropy (MaxEnt) principal are employed.

MaxEnt principal is a stochastic optimization procedure utilizing the Information Theory [Shannon 1948a and 1948b]. Using this principal beside some available information which is formed in a set of constraints one can construct the probability distributions of random coordinates.

Here we summarize what is done in Guilleminot and Soize (2013b) to model a $\mathbb{M}_6^{\mathrm{ti}}(\mathbb{R})$-valued random variable:

6.2.2 Probabilistic Modeling of $\mathbb{M}_6^{ti}(\mathbb{R})$ Random Variable

Let $[\boldsymbol{C}_{clay}^{ti}]$, matrix representation of stochastic consolidated clay elasticity tensor, be a $\mathbb{M}_6^{ti}(\mathbb{R})$-valued second-order random variable, and $[\boldsymbol{N}]$ be the auxiliary $\mathbb{M}_6^{ti}(\mathbb{R})$-valued random variable such that

$$[\boldsymbol{C}_{clay}^{ti}] = (\mathbb{E}\{[\boldsymbol{C}_{clay}^{ti}]\})^{1/2}[\boldsymbol{N}](\mathbb{E}\{[\boldsymbol{C}_{clay}^{ti}]\})^{1/2} \tag{6.5}$$

And

$$\mathbb{E}\{[\boldsymbol{N}]\} = [I], \tag{6.6}$$

$$\mathbb{E}\{\log(\det([\boldsymbol{N}]))\} = \nu, \qquad |\nu| < +\infty \tag{6.7}$$

Following [Guilleminot and Soize 2013b] there exists a matrix $[\boldsymbol{G}]$ ($[\boldsymbol{G}]$ is a random matrix which is unique and symmetric) such that

$$[\boldsymbol{N}] := \mathrm{expm}([\boldsymbol{G}]), \tag{6.8}$$

where expm is the matrix exponential, and

$$[\boldsymbol{G}] = \sum_{i=1}^{5} G_i\left[E_{\mathrm{ti}}^{(i)}\right], \tag{6.9}$$

Now, we define $\boldsymbol{G}$, $\{\boldsymbol{G} := (G_1, G_2, G_3, G_4, G_5)\}$, a $\mathbb{R}^5$ −valued random variable of coordinates on $\mathbb{M}_6^{\mathrm{ti}}(\mathbb{R})$. In the next part, the construction of marginal probability

distributions of random coordinate $\boldsymbol{G}$ (or equivalently random matrix $[\boldsymbol{G}]$) is addressed. Having the probability density functions (pdfs) of $\boldsymbol{G}$, one can construct the pdf of coordinates of $[\mathbf{C}_{clay}^{ti}]$ using Eq. (6.9) and (6.5).

6.2.3 Constructing a Probabilistic Model for Random Variable G

As mentioned earlier, the construction of probability distributions of random variable $\boldsymbol{G}$ is completely equivalent to the construction of the one for random matrix $[\boldsymbol{G}]$. Let define $\{\boldsymbol{g} \rightarrow p_{\boldsymbol{G}}(\boldsymbol{g})\}$ as the family of marginal pdfs of $\boldsymbol{G}$. Two steps are taken in deriving the stochastic model for random variable$\boldsymbol{G}$:

Step 1) Constructing the density $\mathrm{p_G(g)}$

For the MaxEnt formulation, following constraints are considered based on information on $[\boldsymbol{G}]$:

$$\mathbb{E}\left\{\sum_{i=1}^{5} G_i\left[E_{\mathrm{ti}}^{(i)}\right]\right\} = [I], \tag{6.10}$$

$$\mathbb{E}\left\{\log\left(\det\left(\exp\left(\sum_{i=1}^{5} G_i\left[E_{\mathrm{ti}}^{(i)}\right]\right)\right)\right)\right\} = \nu, \qquad |\nu| < +\infty \tag{6.11}$$

By substituting (6.8)-(6.9) in (6.6)-(6.7) one can derive above equations. It can be inferred from Eq. (6.11) that both $[\boldsymbol{N}]$ and $[\boldsymbol{N}]^{-1}$ are second-order random variables [Guilleminot and Soize 2013b]:

$$\mathbb{E}\{\|[\boldsymbol{N}]\|_F^2\} < +\infty \qquad\qquad \mathbb{E}\{\|[\boldsymbol{N}]^{-1}\|_F^2\} < +\infty \tag{6.12}$$

Where $\|[A]\|_F$ is Frobenius norm defined as: as $\|[A]\|_F \coloneqq \ll [A], [B] \gg^{1/2}$.

For the self-readability, we recall here the MaxEnt principle. Let C_{ad} represents the set of all the integrable functions from $\boldsymbol{S} \subseteq \mathbb{R}^5$($\boldsymbol{S}$ is the support of $\boldsymbol{G}$) into $\mathbb{R}^+$ such that satisfies above constraints and let $\varepsilon(p)$ denotes the Shannon measure of entropy of pdf p:

$$\varepsilon(p) = -\int_S p_{\mathbf{G}} l\, n(p_{\mathbf{G}})\, d\boldsymbol{g} \tag{6.13}$$

The MaxEnt then reads:

$$p_{\mathbf{G}} = \arg\max \varepsilon(p) \tag{6.14}$$

$$p \epsilon\, C_{\text{ad}}$$

This method is utilized to obtain the most unbiased probabilistic model for $p_{\mathbf{G}}$. Following [Guilleminot and Soize 2013b], the general solution for the optimization problem (Eq. (6.14)) is obtained as:

$$p_{\boldsymbol{G}}(\boldsymbol{g}) = c^{\boldsymbol{G}} \exp(-\ll [\Lambda^{\text{sol}}], \text{expm}\left(\sum_{i=1}^{5} g_i \left[E_{ti}^{(i)}\right]\right) \gg - \lambda^{\text{sol}} \sum_{i=1}^{5} g_i \,\text{Tr}(\left[E_{ti}^{(i)}\right])) \tag{6.15}$$

where $[\Lambda^{\text{sol}}]$ and λ^{sol} are the unknown Lagrange multipliers and must satisfy constraints (6.10) and (6.11). Following [Guilleminot and Soize 2013b], one can assume $[\Lambda^{\text{sol}}] = \sum_{i=1}^{5} \lambda_i^{\text{sol}} \left[E_{ti}^{(i)}\right]$. It is assumed that the optimization problem is well-posed and the it admits at most one solution. In the sequel, solution Lagrange multipliers will be considered as the vector-valued $\boldsymbol{\lambda}^{\text{sol}} := (\lambda_1^{\text{sol}}, \ldots, \lambda_5^{\text{sol}}, \lambda^{\text{sol}})$.

Step 2) Random generator and definition of G

Let define the potential function, ϕ, from $\mathbb{R}^5$ into $\mathbb{R}$ as [Guilleminot and Soize 2013b]:

$$\phi(\boldsymbol{u}, \boldsymbol{\lambda}) = \ll \sum_{i=1}^{5} \lambda^{(i)} \left[E_{ti}^{(i)}\right], \text{expm}\left(\sum_{i=1}^{5} u_i \left[E_{ti}^{(i)}\right]\right) \gg - \lambda \sum_{i=1}^{5} u_i \,\text{Tr}(\left[E_{ti}^{(i)}\right]) \tag{6.16}$$

and let define $\boldsymbol{Z}_{\boldsymbol{\lambda}}$ as the $\mathbb{R}^5$-valued random variable with the pdf $p_{\boldsymbol{\lambda}}: \mathbb{R}^5 \to \mathbb{R}^+$ given by

$$p_{\boldsymbol{\lambda}}(\boldsymbol{u}) = c_{\boldsymbol{\lambda}} \exp(-\phi(\boldsymbol{u})) \tag{6.17}$$

where $c_{\boldsymbol{\lambda}}$ is a normalization constant. One can deduce that [Guilleminot and Soize 2013b]

$$p_{\boldsymbol{G}}(\boldsymbol{g}) = p_{\boldsymbol{\lambda}^{sol}}(\boldsymbol{g}) \tag{6.18}$$

with $c_{\boldsymbol{\lambda}} = c^{\boldsymbol{G}}$.

Now, let $\{(\boldsymbol{U}(r), \boldsymbol{V}(r)), r \in \mathbb{R}^{+}\}$ be a Markov stochastic process which satisfies the following *ISDE* [Guilleminot and Soize 2013b]:

$$\begin{cases} \mathrm{d}\boldsymbol{U}(r) = \boldsymbol{V}(r)\, dr, \\ \mathrm{d}\boldsymbol{V}(r) = -\nabla_u \phi(\boldsymbol{U}(r); \boldsymbol{\lambda})\mathrm{d}r - \frac{f^0}{2}\boldsymbol{V}(r)\mathrm{d}r + \sqrt{f^0}\mathrm{d}\boldsymbol{W}(r) \end{cases} \tag{6.19}$$

where f^0 belongs to a family of free $\mathbb{R}^{+}$-valued parameters and $\{\boldsymbol{W}(r), r \geq 0\})$ is the $\mathbb{R}^{N}$-valued normalized Wiener process. Following Guilleminot and Soize 2013b we obtain:

$$\lim_{r \to +\infty} \boldsymbol{U}(r) = \boldsymbol{Z}_{\boldsymbol{\lambda}} \tag{6.20}$$

in probability distribution. From (6.18) and (6.20), one can define random variable $\boldsymbol{G}$ as

$$\boldsymbol{G} := \mathcal{H}\,(\{\boldsymbol{W}(r), r \geq 0\})\,, \tag{6.21}$$

Where $\mathcal{H}$ is a non-linear operator.

Following Guilleminot and Soize 2013b, we make use of the Stormer-Verlet algorithm in order to discretize above *ISDE* to sample $\boldsymbol{U}(r)$.

$$\begin{cases} \boldsymbol{U}^{k+\frac{1}{2}} = \boldsymbol{U}^{k} + \frac{\Delta r}{2}\boldsymbol{V}^{k} \\ \boldsymbol{V}^{k+1} = \frac{1-a}{1+a}\boldsymbol{V}^{k} + \frac{\Delta r}{1+a}\boldsymbol{L}^{k+\frac{1}{2}} + \frac{\sqrt{f^0}}{1+a}\Delta\boldsymbol{W}^{k+1} \\ \boldsymbol{U}^{k+1} = \boldsymbol{U}^{k+1/2} + \frac{\Delta r}{2}\boldsymbol{V}^{k+1} \end{cases} \tag{6.22}$$

where $\boldsymbol{U}^{k} = \boldsymbol{U}(r_k)$; $\boldsymbol{V}^{k} = \boldsymbol{V}(r_k)$; $r_k = (k-1)\Delta r$ with Δr represents the sampling step for k=1, 2, …, $M-1$; $a = f^0\frac{\Delta r}{4}$; and $\Delta\boldsymbol{W}^{k+1} = \boldsymbol{W}(r_{k+1}) - \boldsymbol{W}(r_k)$ is the Wiener process increment between r_{k+1} andr_k. $\boldsymbol{u}^1$ and $\boldsymbol{v}^1$ are the initial values for $\boldsymbol{U}$ and $\boldsymbol{V}$, respectively, which are arbitrary deterministic vectors. The $\mathbb{R}^{N}$-valued random variable $\boldsymbol{L}^{k}$ is defined as

$$(\boldsymbol{L}^k)_j = -\{\frac{\partial \phi(\boldsymbol{u};\boldsymbol{\lambda})}{\partial u_j}\}_{\boldsymbol{u}=\boldsymbol{U}^k} \tag{6.23}$$

Following Guilleminot and Soize 2013b, one can deduce that

$$\boldsymbol{G} = \lim_{\Delta r \to 0}(\lim_{k \to +\infty} \boldsymbol{U}(r_k)) \tag{6.24}$$

To generate the samples of $\boldsymbol{U}$ (or as Eq. (6.24) suggests samples of $\boldsymbol{G}$) one needs to find solutions of Lagrange multipliers. For the cubic and isotropic symmetry classes, explicit solutions of Lagrange multipliers can be easily constructed. This is not the case for transversely isotropic class of symmetry. Staber et al. 2015, propose a method to find the approximate solution of Lagrange multipliers which relies on sequential optimization problem. For the class of transversely isotropic symmetry, Lagrange multipliers are:

$$\boldsymbol{\lambda}^{\text{sol}} = -0.8156\big(\delta_{[\boldsymbol{N}]}\big)^{-2.01}(-1,-1,0,-1,-1,1), \tag{6.25}$$

And subsequently

$$\phi(\boldsymbol{u}) = 0.8156\big(\delta_{[\boldsymbol{N}]}\big)^{-2.01}\text{X Tr}(\text{expm}\left(\sum_{i=1}^{5} u_i\left[E_{ti}^{(i)}\right]\right) - \sum_{j=1}^{5} u_j\left[E_{ti}^{(j)}\right]) \tag{6.26}$$

where $\delta_{[\boldsymbol{N}]} := \sqrt{\mathbb{E}\{\|[\boldsymbol{N}] - \mathbb{E}\{[\boldsymbol{N}]\}\|_F^2\}/\|\mathbb{E}\{[\boldsymbol{N}]\}\|_F^2}$ can be calculated using the available experimental data on elasticity matrix $[\mathbf{C}_{clay}^{ti}]$. By substituting (6.26) in (6.23) and using (6.22) one would be able to generate the samples of $\boldsymbol{U}$and subsequently samples of $\boldsymbol{G}$.

Now we aim to construct the pdf of coordinates $\left\{C_i^{clay}\right\}_{i=1}^{5}$ of elasticity tensor $[\mathbf{C}_{clay}^{ti}]$ using the pdf of random variable $\boldsymbol{G}$.

We re-write Eq. (6.9) as:

$$[\boldsymbol{G}] = \{[G_{123}], G_4, G_5\} \tag{6.27}$$

This representation allows for simple algebraic calculation as shown in Walpole (1984). Then, using Eq. (6.8), we obtain

$$[\boldsymbol{N}] := \text{expm}([\boldsymbol{G}]) = \{\text{expm}([G_{123}]), \exp(G_4), \exp(G_5)\} \tag{6.28}$$

And finally using Eq. (6.5) one can generate multiple realizations of $[\boldsymbol{C}]$ using a Monte Carlo simulation.

To find statistical dependency between coordinates$\{C_i\}_{i=1}^{5}$, one can re-write Eq. (6.16) as:

$$p_{\boldsymbol{G}}(\boldsymbol{g}) = p_{G_1, G_2, G_3}(g_1, g_2, g_3) \text{ X } p_{G_4}(g_4) \text{ X } p_{G_5}(g_5) \tag{6.29}$$

Then, using the transformation (5.28) and (5.5) it is deduced that

$$p_{\boldsymbol{C}^{clay}}(\boldsymbol{c}^{clay}) = p_{C_1^{clay}, C_2^{clay}, C_3^{clay}}(c_1^{clay}, c_2^{clay}, c_3^{clay}) \text{ X } p_{C_4^{clay}}(c_4^{clay}) \text{ X } p_{C_5^{clay}}(c_5^{clay}) \tag{6.30}$$

which implies the following:

For the elasticity tensor of consolidated clay belonging to the transversely isotropic class of symmetry, the random coordinates $\{C_i^{clay}\}_{i=1}^{5}$ are such that:

- the components C_1^{clay}, C_2^{clay}, and C_3^{clay} are statistically dependent random variables,
- the components C_4^{clay} and C_5^{clay} are statistically independent (By developing complete equation of $p_{\boldsymbol{C}^{clay}}(\boldsymbol{c}^{clay})$ one can find that C_4^{clay} and C_5^{clay} are Gamma-distributed random variables).

6.3 Probabilistic Developments of a Scalar Parameter

In this section, we aim to construct the probabilistic model for the scalar sources of uncertainty (scalar random variables) in developed microporomechanics model. The

construction of such model is carried out by using the principle of Maximum Entropy (MaxEnt) which has been used in the previous section. Let assume that we aim to construct a probability model for uncertain real-valued parameter x. Then X represents a real-valued random variable with a probability law defined by a pdf $x \to p_X(x)$ on $\mathbb{R}$ which we aim to construct. Following the MaxEnt principal

$$\varepsilon(p) = -\int_s p_{\mathrm{X}} l\, n(p_{\mathrm{X}})\, dx \tag{6.31}$$

Thus, $p_{\mathrm{X}}(x)$ is the pdf of random variable X which probabilistically models the uncertain variable x. Let assume that the available information on x is (i) the support of X, $S_{\mathrm{X}} = [S_1, S_2]$; (ii) the mean value of X, μ_X; and (iii) the dispersion of X, $\delta_X = \frac{\sigma_X}{\mu_X}$, where σ_X represents the standard deviation of X. One can form following equations using available information on x besides using the normalization condition of the $p_{\mathrm{X}}(x)$:

$$\int_{S_X} p_{\mathrm{X}}(x)dx = 1 \tag{6.32}$$

$$\int_{S_X} x\, p_{\mathrm{X}}(x)dx = \mu_X \tag{6.33}$$

$$\int_{S_X} x^2\, p_{\mathrm{X}}(x)dx = (1 + {\delta_X}^2)\, {\mu_X}^2 \tag{6.34}$$

The MaxEnt consists of maximizing the entropy in Eq. (6.31) subjected to the constraints (6.32)-(6.34). The ensuing pdf turns out to be

$$p_X^{\boldsymbol{\lambda}}(x) = \mathbb{1}_S(x)\, \exp(-\lambda_0 - \lambda_1 x - \lambda_2 x^2) \tag{6.35}$$

where $\mathbb{1}_S(x)$ is the characteristic function of S, i.e. $\mathbb{1}_S(x) = 1$ if $x \in S$,0 otherwise; and vector $\boldsymbol{\lambda} = (\lambda_0, \lambda_1, \lambda_2)$ contains the Lagrange multipliers satisfying constraints in Eqs. (44)-(46). $\boldsymbol{\lambda}$ is achieved by minimizing the Hamilton function defined as:

$$\mathcal{H}(\boldsymbol{\lambda}) = \lambda_0 + \lambda_1 \mu_X + \lambda_2 \left(1 + {\delta_X}^2\right) {\mu_X}^2 + \int_{S_X} \exp(-\lambda_0 - \lambda_1 x - \lambda_2 x^2)\, dx \tag{6.36}$$

6.3.1 Random Generator of X

In order to propagate the uncertainty of the uncertain parameter x, we should generate a sufficiently large number, N, of statistically independent realizations of X. To this end, we make use of pseudoinverse method [Devroye L. 1986] to generate realizations of random variable X by utilizing the pdf calculated in the previous part. The N statistically independent realizations of random variable X, $X(a_i)(1 = 1,2, \dots, N)$ can be obtained as following:

$$X(a_i) = \left(F_X^{\lambda}\right)^{-1}\{U(a_i)\} \tag{6.37}$$

where $F_X^{\lambda}(x) = \int_{S_1}^{x} p_X^{\boldsymbol{\lambda}}(\xi)\, \mathrm{d}\xi$ is the c.d.f. (cumulative density function) of X and $U(a_i)$ is a realization of a uniform random variable U with values in S_X.

We construct the pdf and generate independent realizations of scalar uncertain parameters in our model using described methodology.

6.4 Uncertainty Propagation

The algorithm of constructing probabilistic multiscale model of organic rich shale is schematically illustrated in the Fig. 6.1. The construction of probabilistic multiscale model requires substitution of the deterministic vector of input parameters with the random vector of input parameters. Since the input parameters are random, the model outputs will be random as well. Let $\boldsymbol{W}_{level\ I}$ and $\boldsymbol{W}_{level\ II}$ be the random vectors of input parameters at level I and level II. Then, one can show that the elasticity tensor of homogenized medium at level I and level II can be shown by:

at level I: $[\![\boldsymbol{C}]\!]_{hom}^{level\ I} = function_1^{(\boldsymbol{W}_{level\ I})} \quad => f_1\left([\![\boldsymbol{C}]\!]_{hom}^{level\ I}; \boldsymbol{W}_{level\ I}\right) = 0$ (6.38a)

and

at level II: $[\![\boldsymbol{C}]\!]_{hom}^{level\ II} = function_2^{(\boldsymbol{W}_{level\ II}, [\![\boldsymbol{C}]\!]_{hom}^{level\ I})} \Rightarrow f_2([\![\boldsymbol{C}]\!]_{hom}^{level\ II}; \boldsymbol{W}_{level\ II}, [\![\boldsymbol{C}]\!]_{hom}^{level\ I}) = 0$ (6.38b)

In order to solve the above system of stochastic equations, the Monte Carlo simulation is employed. At the first step, for each statistically independent realization of $\boldsymbol{W}_{level\ I}$, statistically independent realization of $[\![\boldsymbol{C}]\!]_{hom}^{level\ I}$ is obtained by solving the Eq. (6.38a). Then, statically independent realizations of $\boldsymbol{W}_{level\ II}$ are used in order to obtain the statically independent realizations of $[\![\boldsymbol{C}]\!]_{hom}^{level\ II}$ by solving Eq. (6.38b).

Finally, statistics on $[\![\boldsymbol{C}]\!]_{hom}^{level\ I}$ and $[\![\boldsymbol{C}]\!]_{hom}^{level\ II}$ are obtained by calculating the statistics on the statically independent realizations of $[\![\boldsymbol{C}]\!]_{hom}^{level\ I}$ and $[\![\boldsymbol{C}]\!]_{hom}^{level\ II}$ obtained from solving the Eqs. (6.38a) and (6.38b).

$for\ itr_i = 1\ to\ N\ (number\ of\ simulations)$

Compute the statically independent realizations of random input vectors

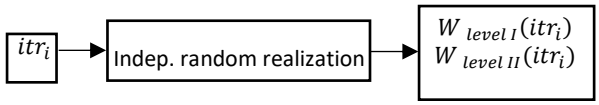

Calculate the elasticity tensor at level I and level II

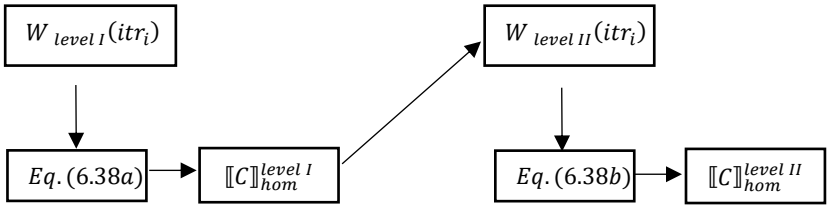

end

Fig. 6.1 Constructing probabilistic multiscale model of organic-rich shale through Monte Carlo simulation

6.5 Chapter Summary

This chapter deals with the construction of a probabilistic multiscale model which quantifies the uncertainties in the uncertain input parameters, and propagates them through multiple length scales to capture the effect of uncertainties on the model output. To this end, a framework of maximum entropy principal and random matrix theory are employed to construct a probabilistic model for the uncertain parameters based on available information. Uncertain parameters are classified as random matrix and random scalar variable, and it is explained in detail how to construct a probabilistic model for both categories, and how to generate samples from those models. Finally, the uncertainties are propagated through different levels using generated samples of uncertain parameters and a Monte Carlo simulation.

7 RESULTS

This chapter is dedicated to the implementation of probabilistic multiscale model developed in previous chapters. First, multiscale model is calibrated using available datasets. Then, values obtained from calibration procedure are validated. Next, an example is given to clarify the construction of probabilistic model at different length scales. Finally, a sensitivity analysis is performed to quantify the contribution of uncertain input parameters to the model output at different length scales.

7.1 Model Calibration

7.1.1 Optimization Problems

The goal of this section is to identify the values of input parameters to our model which cannot be obtained through experiments, or their values cover a wide range and thus it is not easy to determine them based on existing data. Volume fraction of organic and inorganic phases at multiple levels, their corresponding stiffness tensors, the radius of inclusions' grain, and thickness and elasticity properties of ITZ are the input parameters to our model. It is turned out that stiffness tensor of consolidated clay, bulk modulus and Poisson's ratio of kerogen, and thickness and elasticity properties of ITZ cannot be accurately determined from available data. Although some attempts to obtain the stiffness tensor of clay minerals at level 0 have been reported [among others see Alexandrov and Ryzhova 1961; Katahara 1996; Wang et al. 2001], the large range of estimated values for stiffness of clay minerals makes it impossible to choose a value based on these data.

Besides, based on reported values from Monfared and Ulm (2016) and Ortega et al. (2007), stiffness values of consolidated clay at level I is considerably different from those of a single clay mineral.

Thus, a two-step model calibration is performed to determine the mean values of aforementioned input parameters to our model. In step 1, mean values of five independent components of elasticity tensor of consolidated clay at level 0, bulk modulus and Poisson's ratio of kerogen at level I are determined. In step 2, mean values of thickness and elasticity properties of ITZ are determined.

Step 1: In order to find the stiffness tensor of consolidated clay at level I (or equivalently determine five independent components of stiffness tensor of consolidated clay), and bulk and Poisson's ratio of kerogen a downscaling approach is set up. Here, the objective function is to find the values of aforementioned parameters such that Frobenius norm between measured and predicted indentation moduli at level I of samples in CDS 1 would be minimized. The indentation moduli at level I read:

$$\mathrm{M}_3 = 2\sqrt{\frac{C_{11}C_{33}-{C_{13}}^2}{C_{11}}\left(\frac{1}{C_{44}}+\frac{2}{\sqrt{C_{11}C_{33}+C_{13}}}\right)^{-1}} \tag{7.1a}$$

$$\mathrm{M}_1 \approx \sqrt{\sqrt{\frac{C_{11}}{C_{33}}}\frac{{C_{11}}^2-{C_{12}}^2}{C_{11}}\mathrm{M}_3} \tag{7.1b}$$

Following equation represents the minimization problem that is set up to calibrate the multiscale model:

$$min_{\boldsymbol{d}_1}\left(\frac{1}{n_1}\sum\nolimits_{CDS\,1}\left\|M_1^{predicted}-M_1^{measured}\right\|_F+\frac{1}{n_2}\sum\nolimits_{CDS\,1}\left\|M_3^{predicted}-M_3^{measured}\right\|_F\right) \tag{7.2}$$

where n_1 and n_2 are the total number of measurements in samples 108, 150, 151 and Fay with measured values of M_1 and M_3, respectively. Also $\boldsymbol{d}_1 = < C_{11}^{clay}, C_{12}^{clay}, C_{13}^{clay}, C_{33}^{clay}, C_{44}^{clay}, K^{kerogen}, \nu^{kerogen} >$ represents the degrees of freedom associated with the minimization problem. $K^{kerogen}$ represents bulk modulus of kerogen and $\nu^{kerogen}$ denotes Poisson's ration of kerogen. The minimization problem is subjected to a set of constraints to insure the positive definiteness of clay stiffness tensor at level I. These constraints are:

$$C_{11} + C_{12} + C_{33} + \xi > 0 \tag{7.3}$$

$$C_{11} + C_{12} + C_{33} - \xi > 0$$

$$C_{11} - C_{12} > 0$$

$$C_{44} > 0$$

where

$$\xi = \sqrt{{C_{11}}^2 + {C_{12}}^2 + 8{C_{13}}^2 + {C_{33}}^2 + 2C_{11}C_{12} - 2C_{11}C_{33} - 2C_{12}C_{33}} \tag{7.4}$$

In order to perform the optimization problem, a global search in MATLAB using fmincon interior-point optimization algorithm is employed. Obtained values from this optimization problem are used in Step 2 of model calibration in order to find the mean values of thickness of ITZ and its elastic properties.

Step 2: To obtain thickness of ITZ, Δ_{itz}, and its elastic properties (i.e. bulk and shear moduli) a downscaling of macroscopic elasticity of samples in calibration data set 2 (CDS2) is performed. In our model it is assumed that, as mentioned before, ITZ has an isotropic homogeneous behavior whose bulk and shear moduli are set equal to $K^{itz} =$

$C^{itz}K^e$ and $G^{itz} = C^{itz}G^e$ where C^{itz} is a coefficient between 0 and 1 and e denotes equivalent inclusion (self-consistent mixture of quartz and calcite).

Following objective function is set up to obtain the optimum values of parameters:

$$min_{d_2}\left(\sum_{CDS\,2}\left\|[C]^{II,un}_{hom,pred} - [C]^{II}_{measured}\right\|_F\right) \tag{7.5}$$

where $d_2 =< \Delta_{itz}, C^{itz} >$ represents the degrees of freedom associated with the optimization problem, $[C]^{II,un}_{hom,pred}$ denotes predicted undrained stiffness matrix at level II, and $[C]^{II}_{measured}$ is the measured undrained stiffness matrix at level II obtained through UPV measurement.

7.1.2 Input Parameters to Optimization Problems

Implementation of optimization in step 1 requires the volume fraction of consolidated clay, η^{clay}, kerogen, $\eta^{kerogen}$, porosity, φ^{I}, and the values of indentation moduli, M_1 and M_3, for all the samples presented at CDS1. Table 7.1 contains the values of indentation moduli for samples in CDS1. Samples 108, 150,151, and Fay are used to calibrate the model at level I. Also, for the volume fraction of different phases at level I for samples in CDS1 see Table 3.2.

Table 7.1 Calibration Data Set 1 (CDS1) - Indentation Moduli at level I (Abedi et al. 2016a)

Sample	M1	M3
108	28.81 +/- 5.04	19.66 +/- 3.44
	35.3 +/- 6.37	25.17 +/- 4.48
	33.02 +/- 5.74	23.51 +/- 4.24
	30.52 +/- 5.58	…
	34.06 +/- 7.2	…
150	29.1 +/- 5.55	…
151	28.17 +/- 5.39	23.85 +/- 6.22
	29.41 +/- 5.5	23.92 +/- 5.28
	…	23.19 +/- 5.51
Fay	31.99 +/- 5.91	…
	30.27 +/- 6.05	…

For the second optimization problem, Step 2, volume fractions of calcite and quartz grains, $f^{calcite}$ and f^{quartz}, porosity, ϕ^{II}, consolidated clay, f^{clay}, and kerogen, $f^{kerogen}$, at level II and measurements on macroscopic undrained stiffness tensor/matrix of samples in the CDS2 are required. Also, mean values obtained from first optimization problem in Step 1, namely five independent elasticity components of consolidated clay, bulk modulus of kerogen, and Poisson's ratio of kerogen are input parameters to the second optimization problem. Furthermore, inclusion grain radius is another input parameter to this optimization problem. This parameter is obtained through Scanning Electron Microscope (SEM) images of Haynesville shale, and the average inclusion grain radius is considered to be $2\mu m$ [Monfared and Ulm 2016]. Table 7.2 represents five independent components of macroscopic undrained stiffness tensor/matrix of samples B1, B2, and B5 which form CDS2.

Table 7.2 Calibration Data Set 2 (CDS2) - UPV measurements at level II (Monfared and Ulm 2016)

Sample	B1	B2	B5
$\mathbf{C_{11}}$	58.7	54.1	51.4
$\mathbf{C_{12}}$	20.5	19.9	18.3
$\mathbf{C_{13}}$	15.4	11.3	12.6
$\mathbf{C_{33}}$	33.8	33.1	30.3
$\mathbf{C_{44}}$	14.9	15.7	13.6

Table 7.3 contains the volume fractions of phases at level II for samples in Table 7.2.

Table 7.3 Volume fraction of constituent phases for samples presented in CDS2 at level II

sample	f^{clay}	$f^{kerogen}$	f^{quartz}	$f^{calcite}$	ϕ^{II}
B1	0.269	0.05	0.278	0.337	0.066
B2	0.335	0.067	0.246	0.279	0.073
B5	0.384	0.067	0.295	0.182	0.072

All the other volume fractions required for homogenization at level I and level II can be obtained using Table 3.2, Table 7.3 and formulas presented in chapter 5.

7.1.3 Optimization Result

Following the steps mentioned in section 7.1.1 and using the data provided in section 7.1.2 following values are obtained for parameters mentioned in section 7.1.1:

Result from Step 1:

C_{11}^{clay} = 95.6 (GPa), C_{12}^{clay} = 49.6 (GPa), C_{13}^{clay} = 26.5 (GPa)

C_{33}^{clay} = 56.8 (GPa), C_{44}^{clay} = 10.0 (GPa)

$K^{kerogen}$ = 6.35 (GPa), $\nu^{kerogen}$ = 0.28

Result from Step 2:

Δ_{itz} = 0.5 (μm), C^{itz} = 0.5

7.2 Model Validation

In order to validate the result obtained from model calibration, several steps are taken. First, the result obtained for five independent components of elasticity tensor at level 0 are compared to some data available in the literature. Next, result obtained from step 1 of model calibration are employed to predict the indentation moduli of samples in VDS1, and then obtained indentation moduli are compared to their measured counterparts. Finally, result obtained from step 2 of model calibration combined with those from step 1 of model calibration are employed to predict the undrained elasticity tensor/matrix of samples in VDS2, and then are compared to their measured counterparts. Furthermore, an example is presented to validate the probabilistic developments and quantify the role of uncertainty in input parameters of the model on the model output at multiple length scales.

7.2.1 Validation of Consolidated Clay Elasticity Tensor at Level 0

In this section five independent components of stiffness tensor of consolidated clay at level 0 obtained from model calibration are compared to the reported values in the literature. Table 7.4 contains the components of transversely isotropic clay obtained from a combination of experimental techniques. It is clear that except for the value obtained for C_{11}^{clay} from optimization, the values of other components obtained from optimization are compared well with the values reported in Table 7.4. Besides, one needs to take into

consideration that values in Table 7.4 are for individual clay particles at level 0, and not for the consolidated clay at level 0. So, some deviations from stiffness values obtained experimentally are expected as observed by Monfared and Ulm (2016), and Ortega et al. (2007).

Table 7.4 Five independent components of elasticity tensor/matrix of some of the clay particles

Clay Type	C_{11}(GPa)	C_{12}(GPa)	C_{13}(GPa)	C_{33}(GPa)	C_{44}(GPa)
Muscovite(Alexandrov and Ryzhova 1961)	178	42.4	14.5	54.9	12.2
Muscovite(Vaughan and Guggenheim 1986)	184.3	48.3	23.8	59.1	16
Kaolinite(Katahara 1996)	171.5	38.9	26.9	52.6	14.8
Muscovite(Seo et al. 1999)	250	60	35	80	35
Chlorite(Katahara 1996)	181.8	56.8	90.1	96.8	11.4

7.2.2 Validation of Optimization Result at Level I

Values obtained from optimization problem in Step 1 for bulk modulus and Poisson's of kerogen agree well with the data reported in the literature. $K^{kerogen}$ = 6.35 (GPa) is in the range of multiple values reported by Ahmadov et al (2009) and Zeszotarski et al. (2004) for bulk modulus of kerogen. Also, $\nu^{kerogen}$ = 0.28 which is obtained from optimization in Step 1 agrees with the finding of Bousige et al. (2016) which suggests that kerogen's Poisson's ratio is nearly constant ($\upsilon \approx 0.25$) irrespective to its density and state of maturity. To further validate the obtained values through optimization problems,

measured indentation moduli (M_1 and M_3) are plotted against predicted values for samples in VDS1 which are presented in Table 7.5 as well as samples in CDS1.

Table 7.5 Validation Data Set 1 (VDS1) - Indentation Moduli at level I (Abedi et al. 2016a)

Sample	M1	M3
B2	…	23.04 +/- 6.07
	…	22.51 +/- 6.64
	…	24.26 +/- 4.19
	…	24 +/- 7.4
B5	36.83 +/- 6.24	22.84 +/- 7.99
	36.68 +/- 5.68	24.22 +/- 9.33
	28.39 +/- 6.68	22.36 +/- 7.52
	34.8 +/- 6.32	19.85 +/- 6.88
B6	29.68 +/- 7.18	21.09 +/- 5.94
	30.98 +/- 6.22	21.41 +/- 6.75
46	45.74 +/- 9.78	34.59 +/- 8.28
	41.7 +/- 6.3	40.95 +/- 9.58
	53.37 +/- 7.29	37.74 +/- 6.37
	52.61 +/- 7.29	40.5 +/- 7.66
	57.7 +/- 7.1	…
49	50.94 +/- 9.01	…

Table 7.6 contains the volume fractions of samples B2, B5 and B6 in VDS1 at level I. For samples 46 and 49 refer to Table 3.2.

Table 7.6 Volume fraction of constituent phases for samples presented in VDS1 at level I

sample	η^{clay}	$\eta^{kerogen}$	φ^{I}
B2	0.773	0.154	0.073
B5	0.79	0.138	0.072
B6	0.777	0.147	0.076

Fig. 7.1 a) and b) depict this comparison. In these figures, horizontal axis denotes the predicted values and vertical axis denotes experimental measurement. In these graphs measured values denote the average of all the measurements for M_1 or M_3 for each sample. The points with a blue color belong to the CDS1 and the points with a red color belong to VDS1. It is clear from Fig. 7.1 a) and b) that model predictions for M_1 and M_3 is reliable for samples in VDS1 and CDS1.

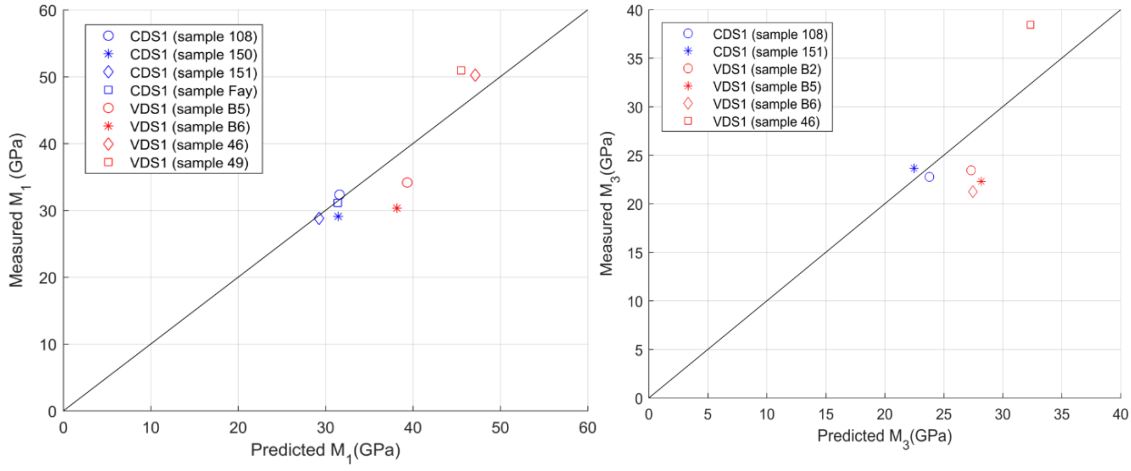

a) b)

Fig 7.1 a) Represents predicted indentation moduli against measured indentation moduli M_1 for both CDS 1 and VDS 1. b) Depicts comparison between predicted and measured indentation moduli M_3 for both CDS1 and VDS1.

7.2.3 Validation of Optimization Result at Level II

In order to validate the result obtained from optimization at level II, predicted components of undrained stiffness tensor are plotted against their counterparts which are obtained through UPV measurements for samples in VDS2, which are shown in Table 7.7, as well as for samples in CDS2.

Table 7.7 Validation Data Set 2 (VDS2) - UPV measurements at level II (Monfared and Ulm 2016)

Sample	B3	B4	B6
$\mathbf{C_{11}}$	49.9	64.6	58.52
$\mathbf{C_{12}}$	13.4	20.3	18.5
$\mathbf{C_{13}}$	10.4	21.4	11.6
$\mathbf{C_{33}}$	41.9	58.7	35.1
$\mathbf{C_{44}}$	15.3	20.7	14.6

Volume fractions of samples in VDS2 are presented in Table 7.8.

Table 7.8 Volume fraction of constituent phases for samples presented in VDS2 at level II

sample	f^{clay}	$f^{kerogen}$	f^{quartz}	$f^{calcite}$	ϕ^{II}
B3	0.103	0.034	0.154	0.663	0.046
B4	0.181	0.055	0.187	0.521	0.056
B6	0.364	0.069	0.276	0.215	0.076

Fig. 7.2 shows this comparison. In this figure, horizontal and vertical axes denote model prediction and measured values, respectively. Blue and red points represent different components of stiffness tensors for samples in CDS2 and VDS2, respectively.

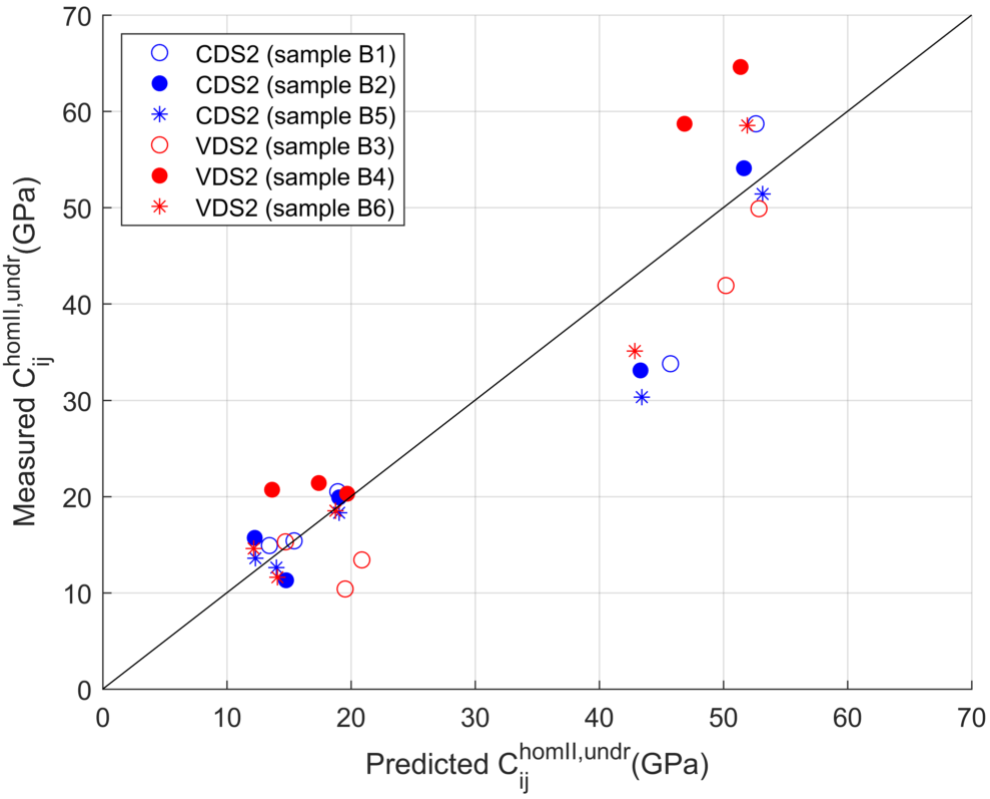

Fig. 7.2 Five independent components of elasticity tensors/matrices at level II for samples in VDS2 and CDS2 obtained from model prediction are plotted against their counterparts obtained through UPV measurements.

7.2.4 Validation of Probabilistic Model at Level I and Level II

In order to quantify the role of uncertainty in input parameters to the model outputs, first one needs to obtain the statistical representation of these parameters and generate realizations from them. To explain this step and as an example, the statistical representation of uncertain input parameters to the model are obtained for sample B6. Stiffness tensor of consolidated clay, volume fractions of clay and kerogen at level I, bulk modulus and Poisson's ratio of kerogen, volume fractions of calcite and quartz at level II, thickness of ITZ and coefficient of elasticity properties of ITZ (C^e) are considered as uncertain input parameters.

Following chapter 6, one can easily generate realizations of components of stiffness tensor of consolidated clay. To this end, we substitute Eq. (6.26) into Eq. (6.23) to obtain $\mathbb{R}^5$-valued random variable $\boldsymbol{L}^k$ (with components $(\boldsymbol{L}^k)_j$ {j $= 1, 2, 3, 4, 5$}) which is a function of $\delta_{[\boldsymbol{N}]}$ and $[E_{ti}^{(i)}]$ $\{i = 1, 2, 3, 4, 5\}$. To obtain $[E_{ti}^{(i)}]$ we need to select $\boldsymbol{n}$, the unit normal orthogonal to the plane of isotropy. It is considered that $\boldsymbol{n}$=(0,0,1) and $\delta_{[\boldsymbol{N}]} = 0.25$. Selected value of $\delta_{[\boldsymbol{N}]}$ represents the uncertainty associated with the elasticity tensor of particles in Table 7.4. Although reported values in Table 7.4 belong to some of the clay particles and not to the consolidated clay at level 0, it is assumed that the uncertainty in elasticity tensor of consolidated clay at level 0 is close to the uncertainty associated with the elasticity tensor of the individual clay particles. Then, we substitute $\boldsymbol{L}^k$ in Eq. (6.22), and set parameters Δr and f^0 equal to 0.001 and 8 respectively. The value of these parameters affects the convergence speed of the discretized *ISDE*. Also, the initial values for $\boldsymbol{U}$ and $\boldsymbol{V}$ are set equal to $\boldsymbol{u}^1 = (0.1,0.2,0.3,0.1,0)$ and $\boldsymbol{v}^1 = 0.5 * \boldsymbol{u}^1$, respectively (initial values for $\boldsymbol{U}$ and $\boldsymbol{V}$ are selected arbitrarily). Eq. (6.22) is an iterative equation. The iterating process should be carried on until the obtained values for $\boldsymbol{U}$ (or as Eq. (6.24) suggests samples of $\boldsymbol{G}$) converges toward the stationary solution of the *ISDE*.

Fig. 7.3 a) displays convergence toward the stationary solution of the *ISDE* for $\Delta r = 10^{-3}$ and Conv-Mes= $\frac{1}{\mathrm{N_{itr}}}\sum_{k=1}^{\mathrm{N_{itr}}}\|U^k\|^2$ where $\mathrm{N_{itr}}$ is the number of iterations and $U^k$is the solution of *ISDE* at iteration k . It is clear that after nearly 1.5x10^6 simulations, the solutions of the *ISDE* are stable. Fig. 7.3 b) depicts the convergence of the means of the five coordinates (elements) of the stationary solution of the *ISDE*, i.e. $\boldsymbol{U} =$

(c_1, c_2, c_3, c_4, c_5) to their stationary values, and Fig. 7.3 c) shows the correlation between five coordinates of the stationary solution of the *ISDE*. As it was expected, there is a high correlation between coordinates c_1, c_2 and c_3 while there is not a considerable correlation between coordinates c_4, c_5 and the rest of the coordinates.

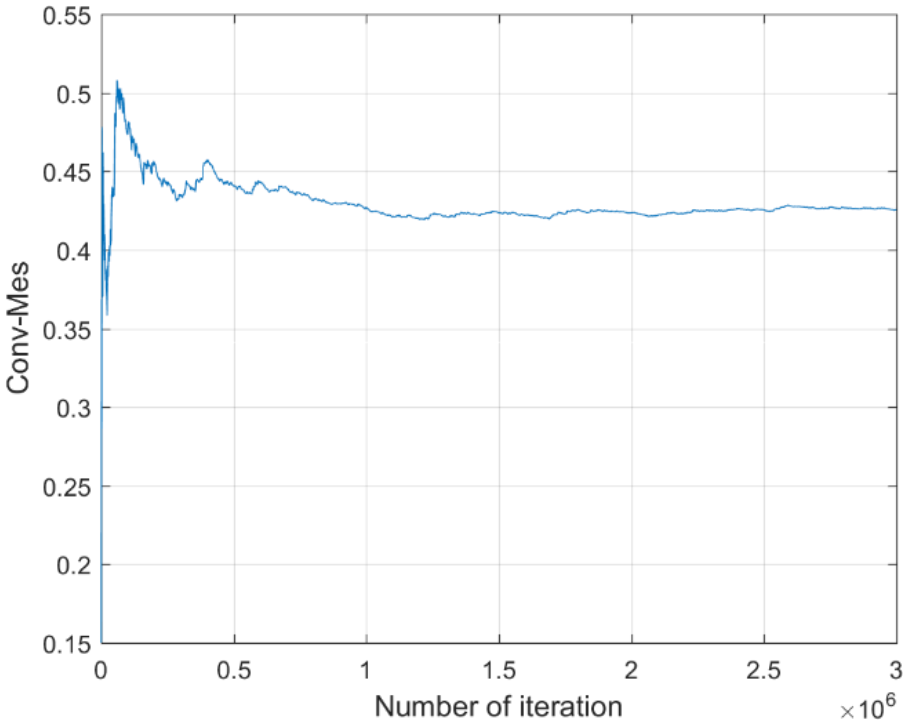

a)

Fig. 7.3 a) Convergence of *ISDE* toward the stationary solution b) Convergence of the mean values of five coordinates (elements) of the *ISDE* solution to the stationary values c) Correlation between five coordinates of the stationary solution of the *ISDE*

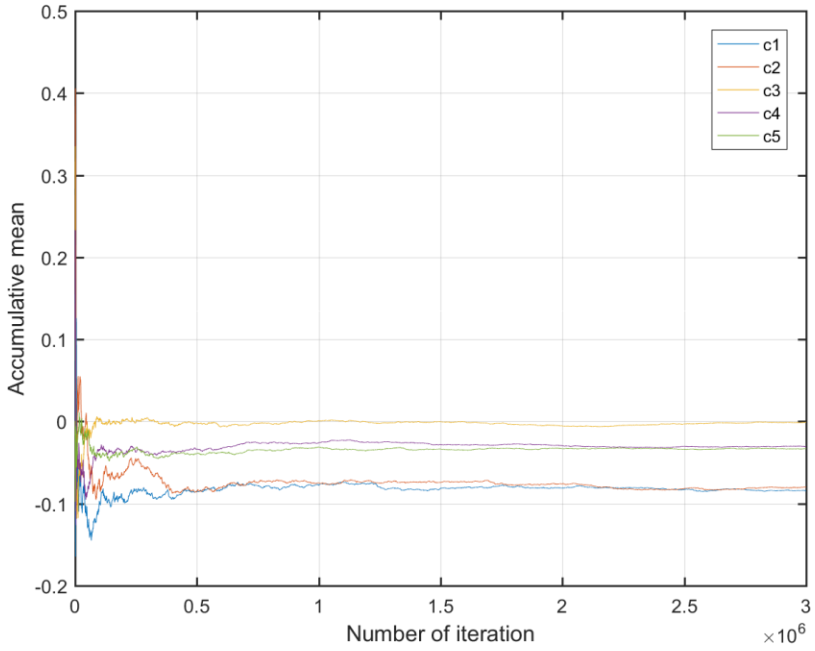

b)

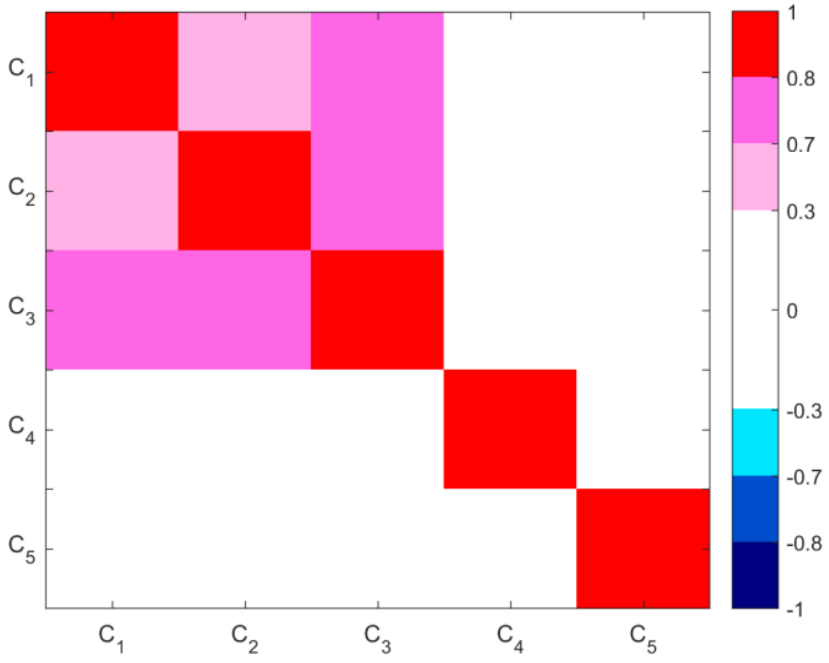

c)

Fig 7.3 Continued.

Next, by having realizations of converged solution of discretized *ISDE* which are practically equal to realizations of $\mathbb{R}^5$-valued random variable $\boldsymbol{G}$, $\{\boldsymbol{G} := (G_1, G_2, G_3, G_4, G_5)\}$ (see Eq. (6.24)), one can obtain realizations of random matrix $[\boldsymbol{G}]$ by substituting realizations of components of $\boldsymbol{G}$ into Eq. (6.9). Subsequently, the realizations of auxiliary $\mathbb{M}_6^{ti}(\mathbb{R})$-valued random variable $[\boldsymbol{N}]$ is obtained by substituting samples of random matrix $[\boldsymbol{G}]$ into Eq. (6.8). Finally, realizations of stochastic stiffness matrix of consolidated clay are obtained by substituting samples of $[\boldsymbol{N}]$ in Eq. (6.5), and setting $\mathbb{E}\{[\boldsymbol{C}_{clay}^{ti}]\}$ equal to the stiffness matrix of consolidated clay obtained from Step 1 of model calibration. Realizations of stochastic stiffness tensor of consolidated clay can be obtained through conversion of generated matrices to corresponding tensors. Fig. 7.4 a) depicts the pdf of component C_{11}^s of stochastic consolidated clay elasticity tensor which is obtained by following the steps mentioned above. To qualitatively evaluate the role of $\delta_{[\boldsymbol{N}]}$ in the resulting pdf of components of stochastic consolidated clay stiffness tensor, Fig. 7.4 b) shows the pdf of component C_{11}^s for three values of $\delta_{[\boldsymbol{N}]}$, namely 0.15, 0.2, and 0.25. It is clear the as $\delta_{[\boldsymbol{N}]}$ increases, support of C_{11}^s becomes wider meaning that the level of uncertainty increases.

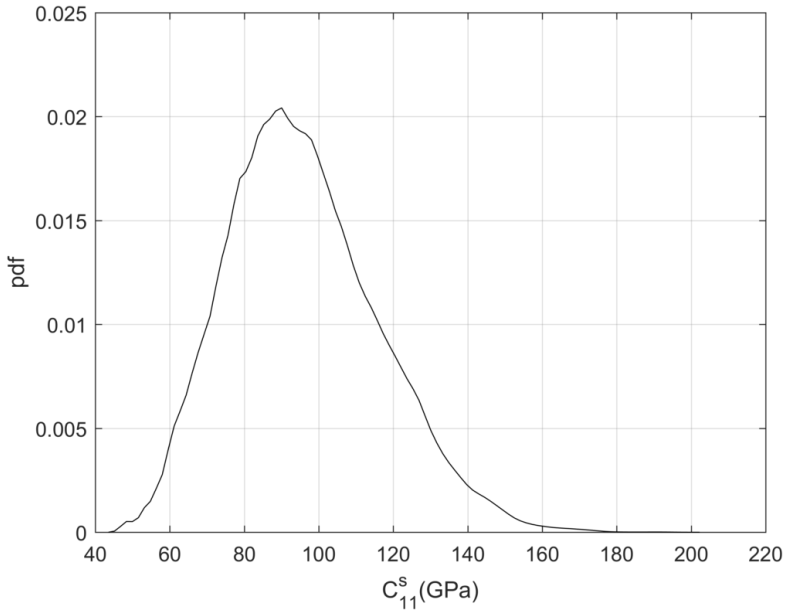

a)

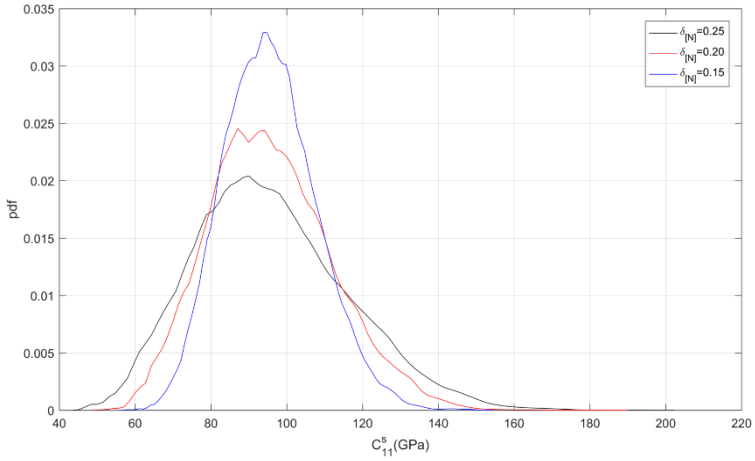

b)

Fig. 7.4 a) Depicts the pdf of component C_{11}^s of the stochastic stiffness tensor of consolidated clay. This pdf is obtained for $\delta_{[N]}$=0.25 and mean value of stochastic stiffness tensor of consolidated clay is equal to the one obtained from Step 1 of model calibration. b) Shows the effect of $\delta_{[N]}$ on the pdf of C_{11}^s. $\delta_{[N]}$ is the only parameter that varies between three curves.

The remaining uncertain parameters to our model are scalar parameters, and based on section 6.3 the information we need to construct their statistical presentation is mean values, supports, and dispersions of these parameters. Table 7.9 summarizes required information for statistical presentation of uncertain scalar parameter:

Table 7.9 Required information on the scalar uncertain parameters for developing their statistical representation

Parameter	Support (S_X)	Mean Value (μ_X)	Dispersion (δ_X)
$\boldsymbol{K^{kerogen}}$	[4, 10]	6.35	0.158
$\boldsymbol{\nu^{kerogen}}$	[0.25, 0.31]	0.28	0.034
$\boldsymbol{\eta^{c}}$	[0.7, 0.84]	0.777	0.034
$\boldsymbol{\eta^{k}}$	[0.13, 0.16]	0.147	0.034
$\boldsymbol{f^{calcite}}$	[0.194, 0.237]	0.215	0.034
$\boldsymbol{f^{quartz}}$	[0.248, 0.304]	0.276	0.034
$\boldsymbol{\Delta_{itz}}$	[0.45, 0.55]	0.5	0.034
$\boldsymbol{C^{itz}}$	[0.45, 0.55]	0.5	0.034

Mean values of $K^{kerogen}$, $\nu^{kerogen}$, Δ^{itz}, and C^{itz} are those obtained from model calibration in section 7.1.1. Mean values of the remaining parameters are set equal to experimental values reported for sample B6. For $K^{kerogen}$, support is obtained from data reported in Ahmadov et al. (2009), and its standard deviation, σ_X, is selected to be 0.83 (it is assumed that the range of support of $K^{kerogen}$ equals $6\sigma_X$), and its dispersion is calculated subsequently ($\delta_X = \frac{\sigma_X}{\mu_X}$). For the remaining parameters, ranges are selected to be [S1, S2], where S1 = (μ_X – (~ 0.1)μ_X) = (μ_X – 3σ_X) and S2 = (μ_X + (~ 0.1)μ_X) = (μ_X + 3σ_X), and dispersion is calculated subsequently ($\delta_X = \frac{\sigma_X}{\mu_X}$).

In order to construct the probabilistic model of uncertain parameters, one needs to determine the Lagrange multipliers associated with each scalar uncertain parameter (see Eq. (6.35)). To this end, one needs to find the set of $(\lambda_0, \lambda_1, \lambda_2)$ for each scalar parameter which minimizes Hamilton function defined by Eq. (6.36). Table 7.10 presents a summary of Lagrange multipliers associated with each of scalar uncertain parameter.

Table 7.10 Estimated Lagrange multipliers for all the scalar uncertain parameters for sample B6

parameter	$\boldsymbol{\lambda_0}$	$\boldsymbol{\lambda_1}$	$\boldsymbol{\lambda_2}$
$\boldsymbol{K^{kerogen}}$	19.28	-5.81	0.46
$\boldsymbol{\nu^{kerogen}}$	409.6	-2952.3	5271.4
$\boldsymbol{\eta^{c}}$	387.7	-1003.9	645.5
$\boldsymbol{\eta^{k}}$	404.3	-5556.6	18889.9
$\boldsymbol{f^{calcite}}$	409.9	-3850.6	8955.9
$\boldsymbol{f^{quartz}}$	410.3	-3000.5	5435.7
$\boldsymbol{\Delta_{itz}}$	410.6	-1654.9	1654.9
$\boldsymbol{C^{itz}}$	410.6	-1654.9	1654.9

Now by substituting estimated Lagrange multipliers in Eq. (6.35), one can construct the pdf of scalar uncertain parameters and subsequently generate independent realizations of these parameters using Eq. (6.38). After generating sufficiently large number of realizations of all the uncertain input parameters to the model, one can construct probabilistic model of stiffness tensors/matrices and poroelastic properties of mature organic-rich shale (Sample B6 in our example) at different levels through Monte Carlo simulation which is described in Fig. 6.1. Fig. 7.5 and Fig. 7.6 represent the results of simulation for sample B6.

Fig. 7.5 a) and b) represent the pdf of indentation moduli M1 and M3 against their measured counterparts for sample B6, respectively. Realizations of M1 and M3 are obtained by employing Eq. (7.1) and realizations of stochastic drained stiffness matrix/tensor of homogenized medium at level I. Fig. 7.6 depicts the pdf of five independent macroscale components of undrained elasticity tensor against their measured counterparts for sample B6. In these graphs, red points show the experimental measurements, and blue vertical lines denote the range of 95% confidence interval region. It is clear that developed model has a good performance in predicting the elasticity properties of sample B6.

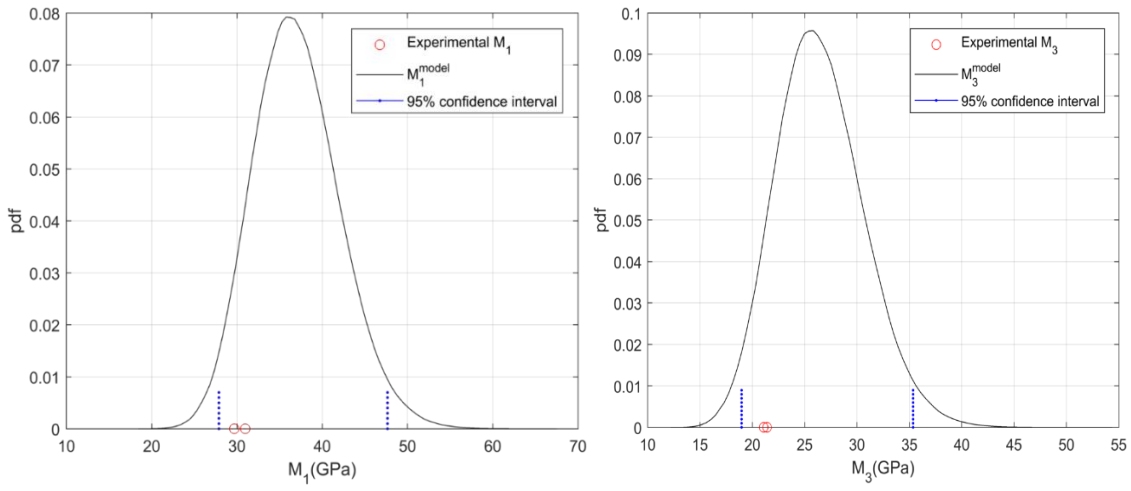

a) **b)**

Fig. 7.5 a) Represents the pdf of M_1 of sample B6 at level I against the measured values of M_1 b) Shows the pdf of M_3 of sample B6 at level I against the measured values of M_3.

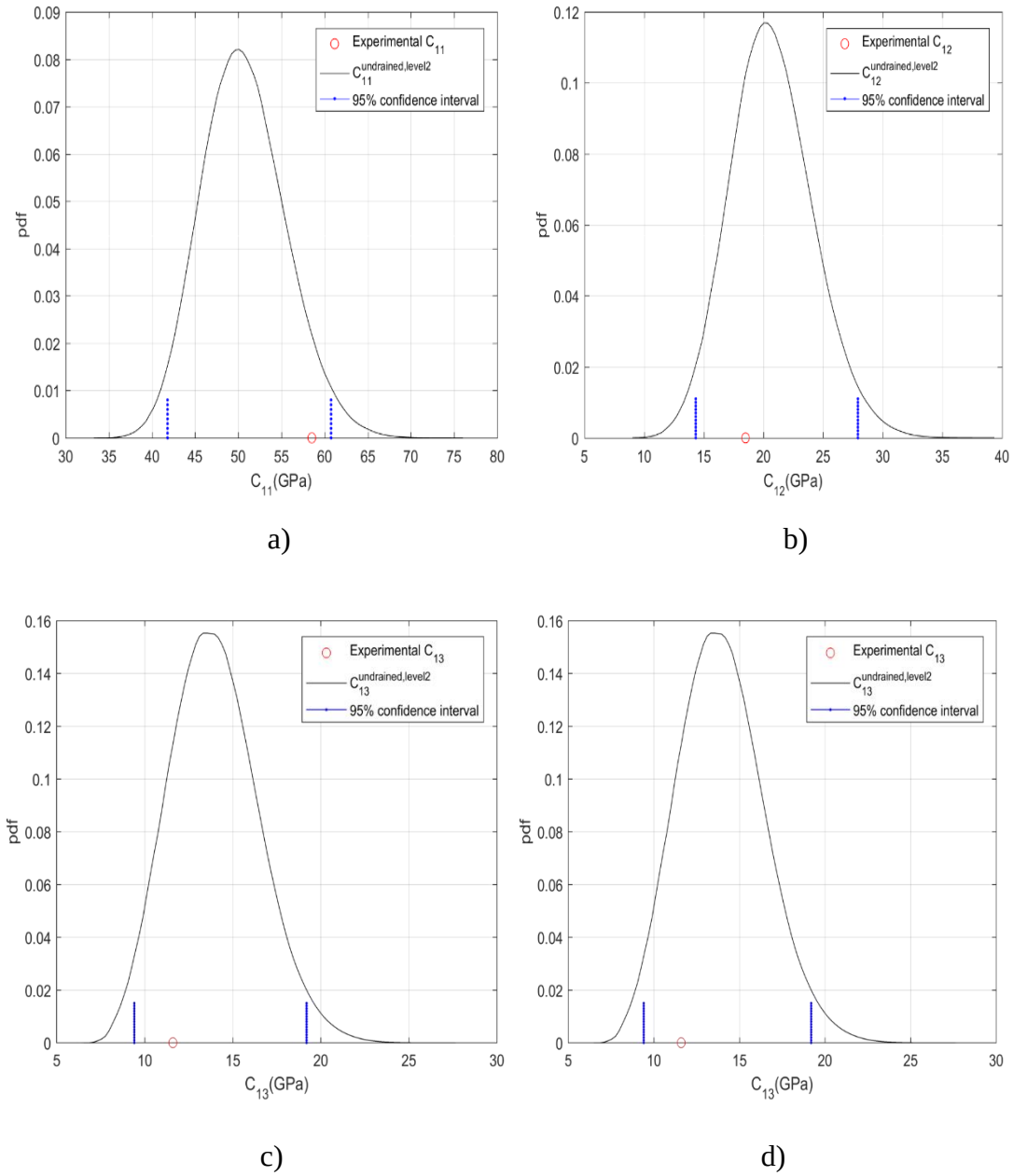

Fig. 7.6 Figures a) through e) represent the pdf of macroscopic undrained components of elasticity tensor of sample B6 against their measured counterparts.

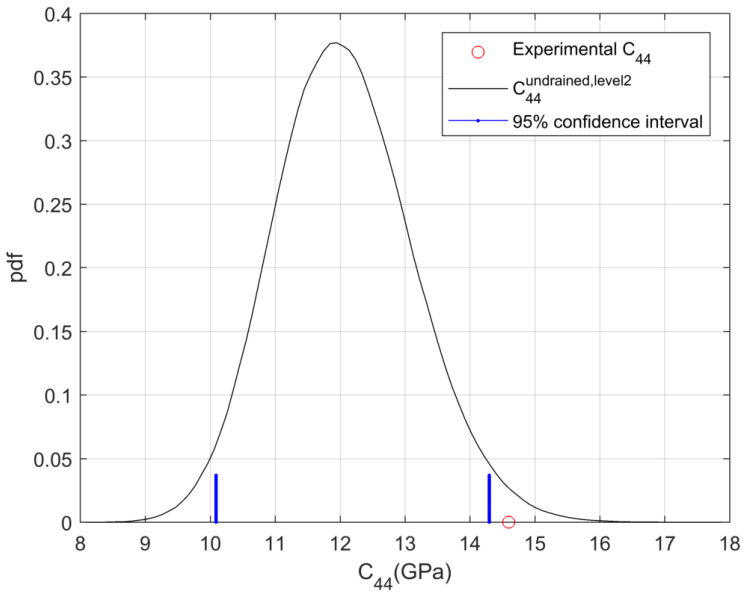

e)

Fig. 7.6 Continued.

To better evaluate the performance of the developed probabilistic model, the standard deviation (as a measure of dispersion) of predicted indentation moduli at level I and predicted components of undrained elasticity tensor at level II are compared to their experimental counterparts. Fig. 7.7 a) depicts the standard deviation of predicted indentation moduli against their experimental counterparts for all the samples in CDS1 and VDS1. In addition, Fig. 7.7 b) represents the standard deviation of predicted undrained components of elasticity tensor at level II for samples in CDS2 and VDS2. In both figures, horizontal axis denotes the predicted values and vertical axis denotes the measured/experimental values. Moreover, horizontal and vertical error bars represent standard deviation of predictions and measurements, respectively.

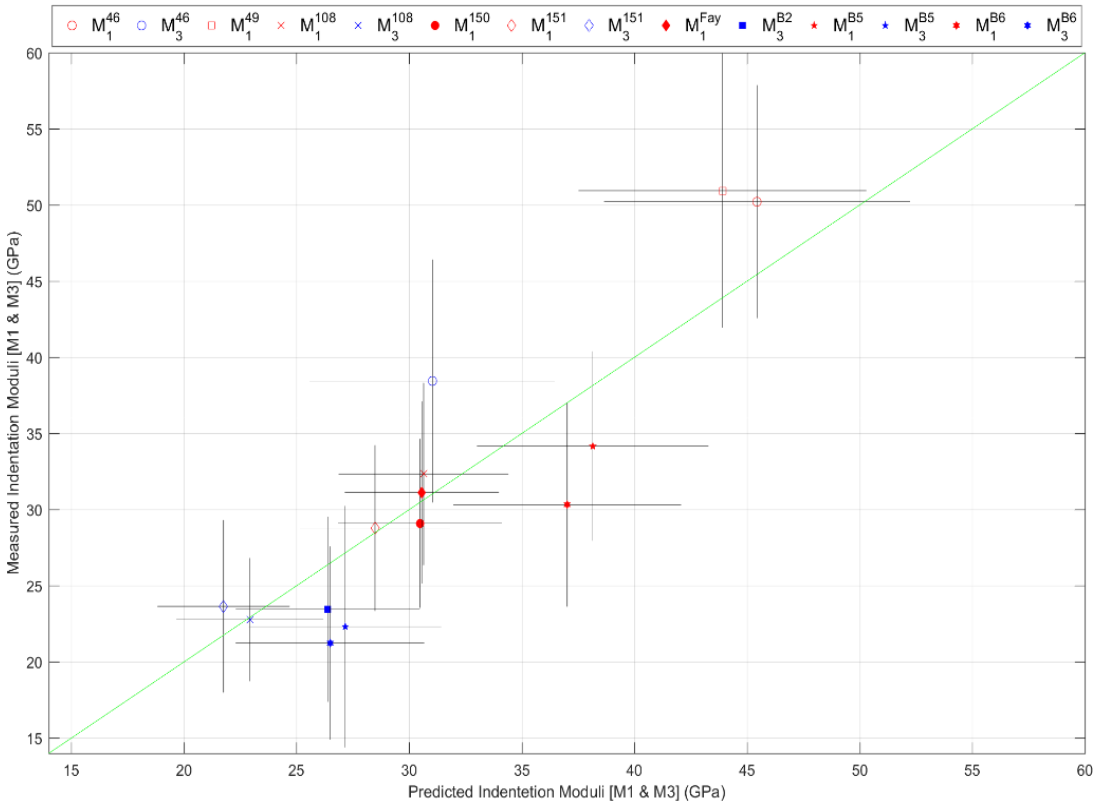

a)

Fig. 7.7 a) Represents standard deviation of predicted indentation moduli for samples in CDS1 and VDS1 against their experimental/measured counterparts b) Depicts the standard deviation of predicted components of undrained stiffness tensor at level II for samples in CDS2 and VDS2. Horizontal and vertical error bars represent standard deviation obtained from predictions and experiments, respectively.

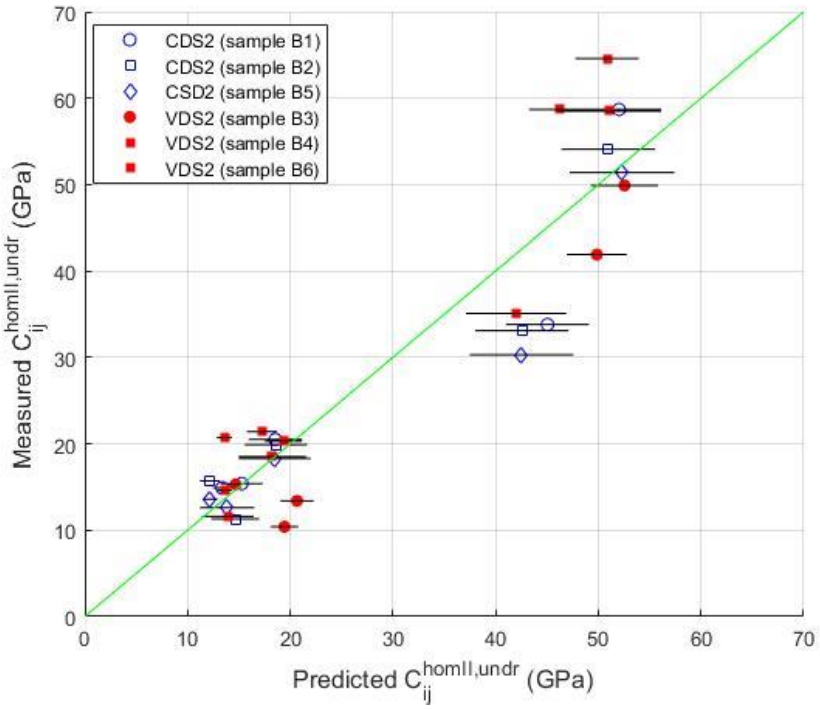

b)

Fig. 7.7 Continued.

7.3 Sensitivity Analysis

To obtain the sensitivity of model output with respect to the uncertainty associated with each uncertain input parameter, Spearman's Rank Correlation Coefficient (SRCC) [Gibbons and Chakraborti, 2003] is employed. Fig. 7.8 a) and b) represent the result of sensitivity analysis at level I and level II respectively. At level I, sensitivity of indentation moduli, M1 and M3, with respect to the variations in the uncertain model input parameters at level I, namely components of clay Elasticity tensor, volume fractions of clay and kerogen, bulk moduli and Poisson's ratio of kerogen is investigated.

At macroscopic length scale, the sensitivity of independent components of undrained elasticity tensor, elasticity moduli ($\mathrm{E_x}$ and $\mathrm{E_z}$), Biot pore pressure coefficients ($\alpha_{11}^{\mathrm{II}}$ and $\alpha_{33}^{\mathrm{II}}$), and the anisotropy parameters [Thomsen 1986] to the variation in uncertain model input parameters, namely thickness of ITZ and coefficient of elasticity properties for ITZ alongside the uncertain parameters considered at level I are studied. The Thomsen parameters ϵ, γ and δ^* as wells as elasticity moduli $\mathrm{E_x}$ and $\mathrm{E_z}$ are defined as:

$$\epsilon = \frac{C_{11}-C_{33}}{2C_{33}} \quad ; \quad \gamma = \frac{C_{66}-C_{44}}{2C_{44}} \quad ; \quad \delta^* = \frac{1}{2C_{33}^2}[2(C_{13}+C_{44})^2 - (C_{33}-C_{44})(C_{11}+C_{33}-2C_{44})]$$

$$\mathrm{E_x} = \frac{1}{\boldsymbol{S}_{11}} = -\frac{-C_{33}C_{11}^2+2C_{11}C_{13}^2+C_{33}C_{12}^2-2C_{12}C_{13}^2}{C_{11}C_{33}-C_{13}^2} \quad ; \quad \mathrm{E_z} = \frac{1}{\boldsymbol{S}_{33}} = \frac{C_{33}(C_{11}+C_{12})-2C_{13}^2}{C_{11}+C_{12}}$$

where $\boldsymbol{S}$ denotes the compliance matrix of undrained elasticity tensor.

It is clear from Fig. 7.8 that volume fraction of clay, η^c, at level I plays a crucial role in the stiffness tensor of model at different length scales compared to volume fractions of other phases. Also, the coefficient of elasticity properties of ITZ, C^{itz}, and thickness of ITZ, Δ_{itz}, do not play a considerable role in the stiffness tensor of model at level II compared to uncertain input parameters at level I and level 0. Furthermore, sensitivity analysis at both levels emphasizes the role of inherent uncertainty in the components of consolidated clay at level 0 on the elastic and poroelastic properties of mature-organic shale at different length scales. To perform the sensitivity analysis, statistically independent realizations of the random input/output parameters generated before are utilized.

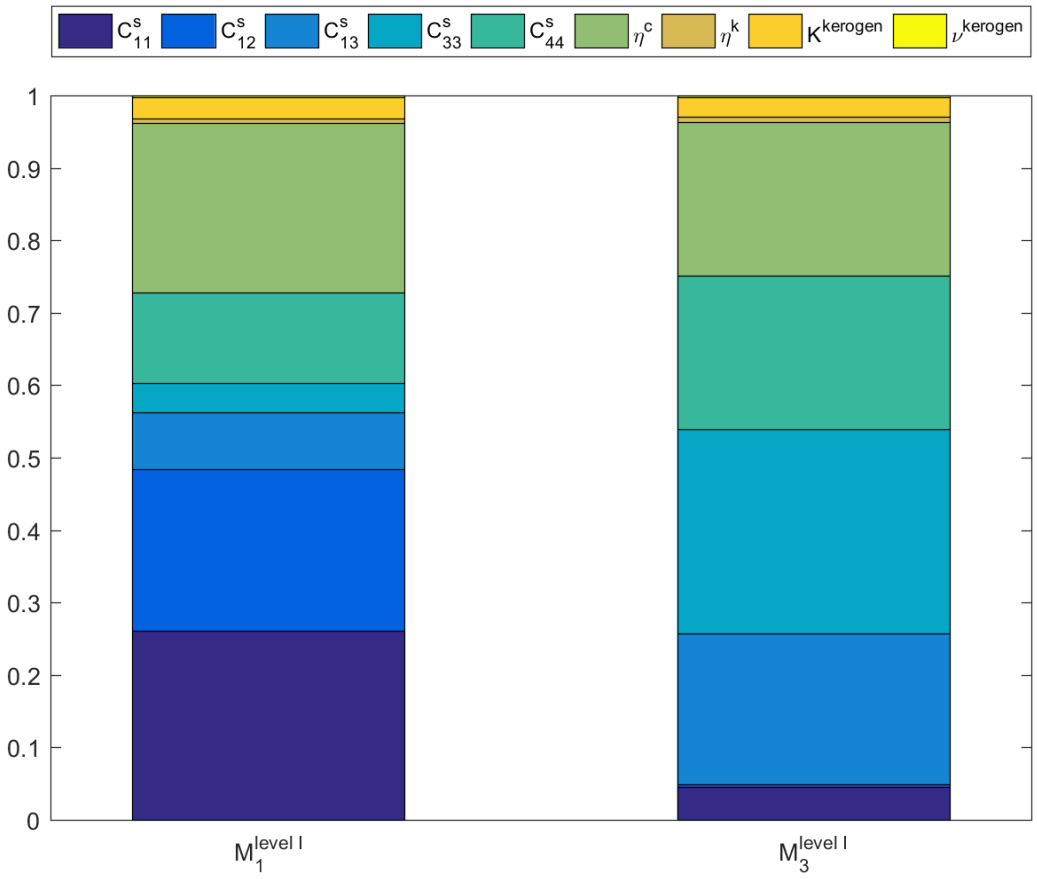

a)

Fig. 7.8 a) Represents the sensitivity analysis of indentation moduli, M_1 and M_3, at level I for sample B6 with respect to components of clay elasticity tensor at level 0, volume fraction of clay, volume fraction of kerogen, bulk modulus and Poisson's ratio of kerogen b) Shows the sensitivity analysis of model outputs at level 2, namely undrained components of elasticity tensor, elastic moduli (E_X *and* E_z), Biot pore pressure coefficients (α_{11}^{II} and α_{33}^{II}) and Thomsen parameters with respect to uncertain input parameters, i.e. thickness of ITZ and coefficient of elastic properties of ITZ alongside the input parameters mentioned for Fig. 7.7 a).

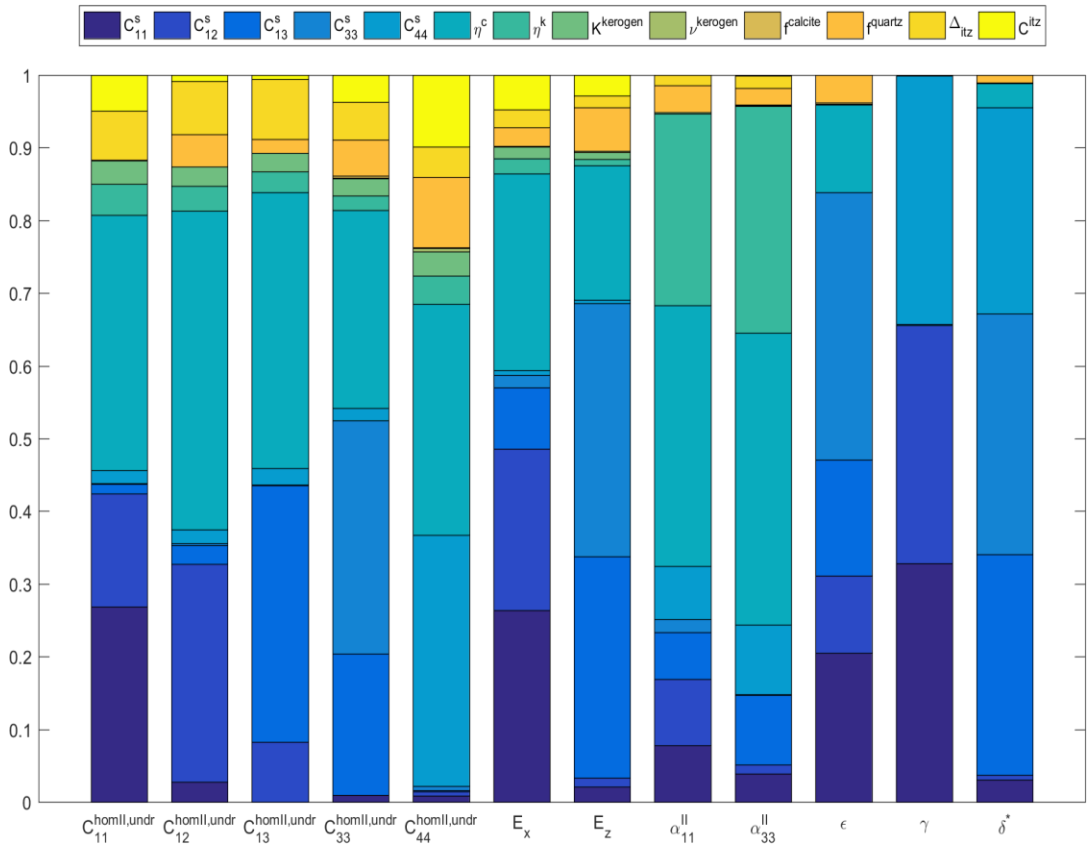

b)

Fig. 7.8 Continued.

7.4 Chapter Summary

This chapter mainly deals with the calibration and validation of developed model. Two datasets at each level are acquired, one for calibration and the other one for validation. Calibration procedure is performed in two steps. In Step 1, components of elasticity tensor of consolidated clay at level 0, bulk modulus of kerogen, and Poisson's ratio of kerogen are obtained through a back-analysis of indentation moduli at level I. In Step 2, properties of ITZ, thickness and elastic properties, are determined through a back-analysis of macroscopic elasticity.

Values obtained from model calibration are compared against available data which emphasizes their validity. To validate the performance of probabilistic developments, elastic properties of sample B6 are obtained by taking into account the uncertainties in the input parameters. It is shown that probabilistic developments in this work are effective in capturing the uncertainties of input parameters and predicting their effects. Finally, a sensitivity analysis is performed to capture the contribution of each uncertain parameter to the model output.

8 CONCLUSION AND FUTURE WORKS

In previous chapters, a probabilistic approach for poroelastic multiscale modeling of organic-rich shale was presented, which accounts for maturity of organic matters and its effect on the morphology of the shale; and weakened interface between inclusion grains and the matrix. Furthermore, it considers the role of uncertainties in input parameters on the model outputs at multiple length scales.

It has been shown that, integrating uncertainty quantification with multiscale modeling of shale can improve the robustness in exploration and exploitation of these highly heterogeneous geomaterials.

8.1 Summary of Main Findings

This work is started with stablishing a multiscale thought model that suites structure and morphology of mature organic-rich shales. Suggested thought model accounts for the self-consistent texture of the mature organic-rich shale, and by introducing the ITZ between inclusion grains and the background matrix, mechanistically models the presence of discontinuity in mature shale. Next, the fundamental rules of microporomechanics are established and employed to develop a multiscale model of organic-rich shale to predict the poroelastic properties of shale. To consider the role of uncertainty in the input parameters of the developed model, a probabilistic framework is constructed to model and quantify the uncertainties in these parameters. Finally,

probabilistic and multiscale models are integrated to develop a probabilistic poroelastic multiscale model for mature organic-rich shale.

Result obtained from model calibration for consolidated clay elasticity tensor agrees well with the reported values in the literature (there is an implicit assumption that components of consolidated clay at level 0 are constant for all the mature organic rich shales from different origins). Also, mean values from model calibration for bulk modulus of kerogen and Poisson's ratio of kerogen is consistent with what is reported in the literature. Additionally, consistency between predicted and measured indentation moduli for two data sets, CDS1 and VDS,1 further verifies the values obtained from optimization problem at level I.

At level II, predicted values for two data sets, CDS2 and VDS2, compare well with the experimental values obtained from UPV measurements. This verifies the obtained values from optimizations at both Steps.

The sensitivity analysis with respect to the uncertainty associated with each uncertain input parameters is performed using Spearman's Rank Correlation Coefficient. This study suggests that at level I, volume fraction of clay has the most important role among volume fraction of presented phases. Also, at level II, components of stiffness tensor of consolidated clay as well as the volume fraction of clay at level I has the most important role in the undrained elasticity tensor of shale. From this analysis, it is clear that the roles of thickness and elasticity properties of ITZs in the Biot pore pressure and Thomsen parameters are negligible compared to other uncertain parameters, which

implies that input parameters associated with ITZs do not serve as a tool to fit predictions to the measurements at level II, but they capture a physical mechanism.

8.2 Limitation and Future Works

The microporomechanics tools used in this work to model the poroelastic behavior of heterogeneous and anisotropic organic-rich shale are limited. For instance, the lack of knowledge about the statistical spatial distribution and orientation of different particles in the composite material serves as an obstacle in better understanding the physics of the problem which translates into a limitation of this model. Also, lack of enough data to capture the uncertainties associated with the uncertain parameters is another limitation of this approach. Having enough data, enables us to quantify uncertainties more accurately, and this will result in a more precise prediction of the quantity of interest.

To improve the model one step forward, the correlation between the amount of different material phases at different length scales can be identified and integrated into the model.

Developed probabilistic multiscale model provides a computationally efficient probabilistic material description that can be used as an input to the computational tools for numerical simulating of fracture behavior of shales at larger scale.

REFERENCES

Abedi, S., Slim, M., Hofmann, R., Bryndzia, T., & Ulm, F. J. (2016a). Nanochemo-mechanical signature of organic-rich shales: a coupled indentation–EDX analysis. *Acta Geotechnica*, 1-14.

Abedi, S., Slim, M., & Ulm, F. J. (2016b). Nanomechanics of organic-rich shales: the role of thermal maturity and organic matter content on texture. *Acta Geotechnica*, 1-13.

Ahmadov, R. (2011). Micro-textural, elastic and transport properties of source rocks. PhD thesis, Stanford University.

Ahmadov, R., Vanorio, T., & Mavko, G. (2009). Confocal laser scanning and atomic-force microscopy in estimation of elastic properties of the organic-rich Bazhenov Formation. *The Leading Edge*, *28*(1), 18-23.

Alexandrov, K. S., & T.V. Ryzhova. (1961). Elastic properties of rock-forming minerals: 2 — Layered silicates: Bulletin of the USSR Academy of Sciences. Geophysical Series, 9, 1165–1168.

Andra 2005, Dossier 2005 Argile: Synthesis. Evaluation of the feasibility of a geological repository in an argillaceous formation. Andra, France. available at: www.andra.fr.

Bobko, C. P., Gathier, B., Ortega, J. A., Ulm, F. J., Borges, L., & Abousleiman, Y. N. (2011). The nanogranular origin of friction and cohesion in shale—a strength homogenization approach to interpretation of nanoindentation results. *International Journal for Numerical and Analytical Methods in Geomechanics*, *35*(17), 1854-1876.

Bobko, C., & Ulm, F. J. (2008). The nano-mechanical morphology of shale. *Mechanics of Materials*, *40*(4), 318-337.

Bousige, C., Ghimbeu, C. M., Vix-Guterl, C., Pomerantz, A. E., Suleimenova, A., Vaughan, G., & Pellenq, R. J. M. (2016). Realistic molecular model of kerogen/'s nanostructure. *Nature materials*, *15*(5), 576-582.

Budiansky, B. (1965). On the elastic moduli of some heterogeneous materials. *Journal of the Mechanics and Physics of Solids*, *13*(4), 223-227.

Cheng, A. D. (1997). Material coefficients of anisotropic poroelasticity. *International Journal of Rock Mechanics and Mining Sciences*, *34*(2), 199-205.

Christensen, R. M., & Lo, K. H. (1979). Solutions for effective shear properties in three phase sphere and cylinder models. *Journal of the Mechanics and Physics of Solids*, *27*(4), 315-330.

Cosenza, P., Prêt, D., Giraud, A., & Hedan, S. (2015). Effect of the local clay distribution on the effective elastic properties of shales. *Mechanics of Materials*, *84*, 55-74.

Cowin, S. C. (2003). A recasting of anisotropic poroelasticity in matrices of tensor components. *Transport in porous media*, *50*(1), 35-56.

Cowin, S. C., & Mehrabadi, M. M. (1992). The structure of the linear anisotropic elastic symmetries. *Journal of the Mechanics and Physics of Solids*, *40*(7), 1459-1471.

Delafargue, A., & Ulm, F. J. (2004). Explicit approximations of the indentation modulus of elastically orthotropic solids for conical indenters. *International Journal of Solids and Structures*, *41*(26), 7351-7360.

Devroye, L. (1986, December). Sample-based non-uniform random variate generation. In *Proceedings of the 18th conference on Winter simulation* (pp. 260-265). ACM.

Dormieux L, Kondo D, Ulm F-J (2006) Microporomechanics.Wiley, Chichester.

Ebrahimi, D., Pellenq, R. J. M., & Whittle, A. J. (2012). Nanoscale elastic properties of montmorillonite upon water adsorption. *Langmuir*, *28*(49), 16855-16863.

Eshelby, J. D. (1957, August). The determination of the elastic field of an ellipsoidal inclusion, and related problems. In *Proceedings of the Royal Society of London A: Mathematical, Physical and Engineering Sciences* (Vol. 241, No. 1226, pp. 376-396). The Royal Society.

Giraud, A., Huynh, Q. V., Hoxha, D., & Kondo, D. (2007). Application of results on Eshelby tensor to the determination of effective poroelastic properties of anisotropic rocks-like composites. *International journal of solids and structures*, *44*(11), 3756-3772.

Guilleminot, J., & Soize, C. (2013a). On the statistical dependence for the components of random elasticity tensors exhibiting material symmetry properties. *Journal of elasticity*, *111*(2), 109-130.

Guilleminot, J., & Soize, C. (2013b). Stochastic model and generator for random fields with symmetry properties: application to the mesoscopic modeling of elastic random media. *Multiscale Modeling & Simulation*, *11*(3), 840-870.

Hellmich, C., Barthélémy, J. F., & Dormieux, L. (2004). Mineral–collagen interactions in elasticity of bone ultrastructure–a continuum micromechanics approach. *European Journal of Mechanics-A/Solids*, *23*(5), 783-810.

Hershey, A. V. (1954). The elasticity of an isotropic aggregate of anisotropic cubic crystals. *Journal of Applied mechanics-transactions of the ASME*, *21*(3), 236-240.

Hill, R. (1965). A self-consistent mechanics of composite materials. *Journal of the Mechanics and Physics of Solids*, *13*(4), 213-222.

Hornby, B. E., Schwartz, L. M., & Hudson, J. A. (1994). Anisotropic effective-medium modeling of the elastic properties of shales. *Geophysics*, *59*(10), 1570-1583.

Katahara, K.W. (1996). Clay mineral elastic properties. SEG Technical Program, Expanded Abstracts, 15, 1691–1694.

Kröner, E. (1958). Berechnung der elastischen Konstanten des Vielkristalls aus den Konstanten des Einkristalls. *Zeitschrift für Physik*, *151*(4), 504-518.

Laws, N., & Dvorak, G. J. (1987). The effect of fiber breaks and aligned penny-shaped cracks on the stiffness and energy release rates in unidirectional composites. *International Journal of Solids and Structures*, *23*(9), 1269-1283.

Mavko, G., Mukerji, T., & Dvorkin, J. (2009). *The rock physics handbook: Tools for seismic analysis of porous media*. Cambridge university press.

Monfared, S. (2015). Microporoelastic modeling of organic-rich shales. MSc thesis, MassachusettsInstitute of Technology.

Monfared, S., & Ulm, F. J. (2016). A molecular informed poroelastic model for organic-rich, naturally occurring porous geocomposites. *Journal of the Mechanics and Physics of Solids*, *88*, 186-203.

Mori, T., & Tanaka, K. (1973). Average stress in matrix and average elastic energy of materials with misfitting inclusions. *Acta metallurgica*, *21*(5), 571-574.

Mura, T. (2013). *Micromechanics of defects in solids*. Springer Science & Business Media.

Ortega, J.A. (2010). Microporomechanical Modeling of Shale. PhD thesis, Massachusetts Institute of Technology.

Ortega, J. A., Ulm, F. J., & Abousleiman, Y. (2007). The effect of the nanogranular nature of shale on their poroelastic behavior. *Acta Geotechnica*, *2*(3), 155-182.

Ortega, J. A., Ulm, F. J., & Abousleiman, Y. (2009). The nanogranular acoustic signature of shale. *Geophysics*, *74*(3), D65-D84.

Passey, Q. R., Bohacs, K., Esch, W. L., Klimentidis, R., & Sinha, S. (2010, January). From oil-prone source rock to gas-producing shale reservoir-geologic and petrophysical characterization of unconventional shale gas reservoirs. In *International oil and gas conference and exhibition in China*. Society of Petroleum Engineers.

Prasad, M., Mukerji, T., Reinstaedler, M., & Arnold, W. (2009, January). Acoustic signatures, impedance microstructure, textural scales, and anisotropy of kerogen-rich shales. In *SPE annual technical conference and exhibition*. Society of Petroleum Engineers.

Rice, J. R., & Cleary, M. P. (1976). Some basic stress diffusion solutions for fluid-saturated elastic porous media with compressible constituents. *Reviews of Geophysics*, *14*(2), 227-241.

Robinet, J. C., Sardini, P., Coelho, D., Parneix, J. C., Prêt, D., Sammartino, S., & Altmann, S. (2012). Effects of mineral distribution at mesoscopic scale on solute diffusion in a clay-rich rock: Example of the Callovo-Oxfordian mudstone (Bure, France). *Water Resources Research*, *48*(5).

Sansalone, V., Gagliardi, D., Desceliers, C., Bousson, V., Laredo, J. D., Peyrin, F., & Naili, S. (2016). Stochastic multiscale modelling of cortical bone elasticity based on high-resolution imaging. *Biomechanics and modeling in mechanobiology*, *15*(1), 111-131.

Sarout, J., & Guéguen, Y. (2008). Anisotropy of elastic wave velocities in deformed shales: Part 1—Experimental results. *Geophysics*, *73*(5), D75-D89.

Sayers, C. M. (1994). The elastic anisotrophy of shales. *Journal of Geophysical Research: Solid Earth*, *99*(B1), 767-774.

Sayers, C. M. (2005). Seismic anisotropy of shales. *Geophysical prospecting*, *53*(5), 667-676.

Seo, Y. S., Ichikawa, Y., & Kawamura, K. (1999). Stress-strain response of rock-forming minerals by molecular dynamics simulation. Mater. Sci. Res. Int. 5, 13-20.

Shannon, C.E. (1948a). A mathematical theory of communication. Bell Syst. Tech. J. 27, 379–423.

Shannon, C.E. (1948b). A mathematical theory of communication. Bell Syst. Tech. J.27, 623–659.

Skempton, A. W. (1984). The pore-pressure coefficients A and B. In *Selected Papers on Soil Mechanics* (pp. 65-69). Thomas Telford Publishing.

Staber, B., & Guilleminot, J. (2015). Approximate solutions of Lagrange multipliers for information-theoretic random field models. *SIAM/ASA Journal on Uncertainty Quantification*, *3*(1), 599-621.

Thomsen, L. (1986). Weak elastic anisotropy. *Geophysics*, *51*(10), 1954-1966.

Tourtelot, H. A. (1960). Origin and use of the word "shale". *American Journal of Science*, *258*, 335-343.

Ulm, F. J., & Abousleiman, Y. (2006). The nanogranular nature of shale. *Acta Geotechnica*, *1*(2), 77-8.

Vasin, R. N., Wenk, H. R., Kanitpanyacharoen, W., Matthies, S., & Wirth, R. (2013). Elastic anisotropy modeling of Kimmeridge shale. *Journal of Geophysical Research: Solid Earth*, *118*(8), 3931-3956.

Vaughan, M. T., & Guggenheim, S. (1986). Elasticity of muscovite and its relationship to crystal structure. *Journal of Geophysical Research: Solid Earth*, *91*(B5), 4657-4664.

Vernik, L., & Landis, C. (1996). Elastic anisotropy of source rocks: Implications for hydrocarbon generation and primary migration. *AAPG bulletin*, *80*(4), 531-544.

Vernik, L., & Liu, X. (1997). Velocity anisotropy in shales: A petrophysical study. *Geophysics*, *62*(2), 521-532.

Walpole, L. J. (1984, January). Fourth-rank tensors of the thirty-two crystal classes: multiplication tables. In *Proceedings of the Royal Society of London A: Mathematical, Physical and Engineering Sciences* (Vol. 391, No. 1800, pp. 149-179). The Royal Society.

Wang, Z., Wang, H., & Cates, M. E. (2001). Effective elastic properties of solid clays. *Geophysics*, *66*(2), 428-440.

Withers, P. J. (1989). The determination of the elastic field of an ellipsoidal inclusion in a transversely isotropic medium, and its relevance to composite materials. *Philosophical Magazine A*, *59*(4), 759-781.

World Energy Council (2007) Survey of energy resources. Technical report. World Energy Council.

Zaoui, A. (2002). Continuum micromechanics: survey. *Journal of Engineering Mechanics*, *128*(8), 808-816.

Zeszotarski, J. C., Chromik, R. R., Vinci, R. P., Messmer, M. C., Michels, R., & Larsen, J. W. (2004). Imaging and mechanical property measurements of kerogen via nanoindentation. *Geochimica et cosmochimica acta*, *68*(20), 4113-4119.